Endosymbiotic bioenergetic synergy behind climate-mediated species boundaries of rainforest warblers

Dahong Chen[1] and Silu Wang[2]

[1] Department of Biochemistry, Jacobs School of Medicine & Biomedical Sciences, State University of New York, Buffalo

[2] Department of Biological Sciences, State University of New York, Buffalo

co-corresponding author email: siluwang.biodiv@gmail.com

Abstract

The molecular cooperation among organelles facilitates adaptation during eukaryotic evolution, but the role of endosymbiotic synergy in the organismal climate adaptation remains unclear. Here we unveil the Endosymbiotic Bioenergetic Synergy Model, which characterizes the role of emergent molecular activities among organelles underlying energy metabolism in climate adaptation of eukaryotes. The hybridizing wood warblers experiencing dramatic climate changes in the Pacific Northwest provide natural recombination experiments to understand the molecular genomic responses to climate change. Integrating life history morphometrics, cell-type-specific multiomics, biochemical analyses and confocal imaging, we discovered the endosymbiotic bioenergetic synergy among nucleus, mitochondria, and ribosome at the molecular foundation of climate adaptation. We further elucidated adaptive inertia in the forms of oxidative stress and OXPHOS inefficiency that can be partially alleviated by the introgression of warm-adapted endosymbiotic genetic variants across the species boundaries. This synergistic insight in endosymbiotic bioenergetics has broad implication for understanding eukaryotic cells over space and time.

Introduction

Cytonuclear coevolution facilitates organismal adaptation on our changing planet since the endosymbiotic origin of eukaryotes over 2 billion years ago (Sagan 1967; Betts et al. 2018; Raval et al. 2024). Such ancient and evolving coordination of molecular activities among organelles, or 'endosymbiotic synergy', underpins the core bioenergetic functions of eukaryotic cells (Swerdlow, 2016). However, the cooperating molecular partners of heterogenous origins are prone to conflicts of interests, genealogical discordance, and potential incompatibility across the species boundaries (Sloan et al. 2017; Hill, 2017; Wang et al., 2021, Moran et al. 2025; Wang et al. 2025) and/or changing environment (Quirós et al. 2016; Burton, 2022; Sokolova, 2023; Keefe, et al. 2025). Therefore, the evolving synergy among endosymbiotic molecular partners can be central to climate adaptation in the rapidly changing world, yet we are merely beginning to understand the synergy behind the organismal responses to climate change, particularly in natural habitats (Raval et al. 2024). Here we propose the 'Endosymbiotic Bioenergetic Synergy Model', which characterizes the coordination of molecular activities among organelles involved in energy metabolism as a fundamental evolutionary step towards climate adaptation in eukaryotic organisms.

Much progress has been made in understanding the bioenergetic response to environmental variation, but the sum of individual molecular processes is insufficient to explain the collective outcome, considering the functional complexity emerged among their interactions (Sokolova, 2023; Kim & Lee, 2024; Keefe, et al. 2025). Therefore, the emergent property in the endosymbiotic interactions remains a knowledge gap for understanding the molecular mechanisms underlying organismal climate adaptation (Sokolova, 2023; Keefe, et al. 2025). The mitochondrial oxidative phosphorylation (OXPHOS) machinery at the core of animal bioenergetics is jointly encoded by nuclear and mitochondrial genomes, and coordinatively translated and maintained by mitoribosomes and cytoribosomes (Mai 2017; McShane et al., 2024; Antolínez-Fernández et al. 2024). It is well known that mitochondrial biogenesis (Liu and Brooks, 2012; Medeiros, 2008; Popov, 2020; Keefe, et al. 2025), ribosomal function (Sonenberg, N., & Hinnebusch, 2009; Rahaman et al. 2025), and OXPHOS activity (Liu and Brooks, 2012; Salgado et al., 2017; Patton et al., 2018; Sokolova, 2023) cooperate and respond to thermal changes with different sensitivity (Sokolova, 2023). Accordingly, heat-stress often results in oxidative stress and OXPHOS disorders (Cao et al. 2023; Larsen et al. 2012). In contrast, heat acclimation is known to induce stronger ribosomal responses (Gerashchenko et al. 2012), increased protein content in Complexes I-V of OXPHOS (Tamura et al. 2014), higher OXPHOS efficiency (Salgado et al. 2017; Patton et al. 2018) and elevated mitochondrial biogenesis that strengthen mitochondrial energy production. Therefore, heat acclimation opens the opportunity to promote endosymbiotic

efficiency and long-term heat adaptation. Remarkably, the mechanistic understanding of heat acclimation is currently missing for long-term studies of natural habitats (Keefe et al. 2025). Naturally hybridizing species that divergently adapt along a climatic gradient provide acclimation and recombination experiments to uncover such molecular genetic basis of long-term climate adaptation.

Wood warblers *Setophaga occidentalis* (SOCC) and *S. townsendi* (STOW) breed in the canopy of the coniferous forests along western North America and provide a unique opportunity to determine the molecular basis of climate adaptation in a natural context (Fig. 1A-D; Wang et al. 2021). STOW breeds in the cooler and dryer inland coniferous forests of Douglas Firs, Western Hemlocks, Ponderosa Pines (Fig. 1E), while SOCC breeds in the southern warmer and humid coastal rainforests of Douglas Firs, Western Hemlocks Giant Sequoia, and Coastal Redwoods (Fig. 1F). SOCC and STOW are at the early stage of speciation with three hybrid zones, one of which is in Sister, Oregon that went through drastic environmental changes over the past two decades (Rohwer & Wood, 1998; Wang et al. 2019, 2020, De Zwaan et al. 2022).

This wood warbler species complex provides a unique system to investigate the Endosymbiotic Bioenergetic Synergy Model. SOCC and STOW exhibit distinct mitochondrial haplotypes (Krosby & Rohwer 2009) with a significant signature of divergent selection in NADH dehydrogenase and ATP synthase (Fig. 1L-M) (Wang et al. 2021). The distinct mitochondrial haplotypes coexist in ancient hybrid populations (Wang et al. 2019) and coevolve with a nuclear gene block enriched for lipid metabolism (Wang et al. 2021). Furthermore, the mitonuclear ancestries covary with climatic variations across coastal British Columbia and Alaska, indicating climate adaptation through mitonuclear coevolution (Wang et al. 2021). Notably, the endosymbiotic molecular interactions behind their climate adaptation remain uncharacterized.

Here we integrate blood cell bioenergetics, multiomics and life history morphometrics (Fig. 1K) to reveal the molecular basis of organismal climate adaptation in response to the climate changes between 1970-2000 and 2024. We ask: (1) how does the endosymbiotic bioenergetic complex contribute to climate adaptation; (2) does this complex display molecular signatures of adequate response or adaptive inertia to dramatic climate changes; (3) whether the historically warm-adapted SOCC exhibits endosymbiotic energetics of hot acclimation, featuring higher OXPHOS activities and efficiency relative to the cold-adapted STOW; (4) whether the mismatched ancestries of endosymbiotic genes lead to compromised synergy and bioenergetics; (5) would the warm-adapted SOCC variants adaptively introgress across the species boundary? To infer the emergent property of these endosymbiotic molecular responses, we build an

integrative framework to predict the coordinated synergy of molecular activities behind organismal responses to climate change.

Results

Climate change and life history adaptation

The breeding habitats of SOCC, hybrids, and STOW partition along a climatic gradient from the historically warmer and humid SOCC temperate rainforests along coastal Oregon and California, to the cooler and drier forests of STOW in eastern Oregon, Idaho, and Montana in 1970-2000 (Fig. 1A-F). The loss of old growth forests (Fig. 1I) in concert with the rapid climate changes over the past two decades (Fig. 1G) reshaped the climatic gradient of SOCC and STOW habitats. The inland STOW breeding habitats have become drastically dryer and invertedly warmer than the SOCC habitats (Fig. 1G). Remarkably, the temperature of the STOW habitats increased by 5.85 °C ($p < 10^{-6}$) with a reduction of monthly precipitation by 12.86 mm ($p < 10^{-4}$) in the 2024 breeding season relative to the 1970-2000 average. Severe climate changes also occurred to the hybrid habitat in Sister, Oregon with a temperature increase by 3.68 °C ($p < 10^{-7}$) and a monthly average precipitation drop by 8.24 mm ($p < 10^{-9}$) in 2024 over 1970-2000 (Fig. 1G). Despite the coastal location, SOCC habitats displayed a mild but concerning trend of a mean temperature increase by 0.42 °C ($p > 0.05$) and a mean monthly precipitation decline by 2.17 mm ($p > 0.05$) (Fig. 1G). Furthermore, the vapor pressure (VP) significantly changed in all habitats, with an average increase of 0.16 Kpa ($p < 10^{-7}$) for SOCC, 0.17 ($p < 10^{-12}$) for STOW, and 0.29 ($p < 10^{-14}$) for hybrids (Fig. 1G). These changes became particularly dramatic between 2000-2024, coincident with the massive loss (over 8 million hectares cumulatively) of old-growth western forests (Fig. 1I). These rapid and catastrophic climate changes pose challenges to climate adaptation of wildlife.

Integrating climate data and field measurements, we found that the life-history morphometrics of adult breeding warblers represents significant signatures of climate adaptation (Fig. 1J-K). The historical temperature of breeding seasons remarkably predicts the morphometric PC1 ($r = 0.30$, $p = 0.031$, Fig. 1J-K), which represents 28.2% of the total variation and reflects different beak shapes and sizes (Fig. 1J-K). Birds with bigger beaks partition to warmer breeding habitats (Fig. 1J-K), implying bigger preys in a warmer environment. PC2 represents 22.1% of the total variation, primarily reflecting wing size differences (Fig. 1K), and positively correlates with precipitation ($r = 0.30$, $p = 0.035$) of the breeding season. A larger wing surface area is known to compensate the density of humid air for aerodynamic lift (Pennycuick, 1975; Swartz et al. 2008),

whereas a smaller wing surface in drier habitats could be adaptive to reduce water loss (Muñoz-Garcia et al. 2016). Remarkably, the life history morphometric axis significantly associates with historical but not recent climate conditions (Fig. 1J-K). This contrast indicates adaptive inertia or potential maladaptation, considering the inverted temperature gradient between SOCC and STOW habitats in the recent decades (Fig. 1G).

Endosymbiotic molecular basis of climate adaptation

We performed multiomic analyses and identified endosymbiotic genes at the molecular frontiers that coordinate nucleus, mitochondria, cyto-ribosomes, and mito-ribosomes behind the observed climate adaptation. Using blood cells of breeding adults, we conducted Nanopore sequencing, Illumina whole genome sequencing, and RNA-seq analyses to establish genome references and annotations, determine species-specific genotypes, and identify genes and signaling pathways that are differentially expressed among SOCC, hybrids, and STOW (see Methods). Transcriptomic analyses identified 2,037 differentially expressed genes between SOCC and STOW after ancestry normalization, with hybrids displaying intermediate expression (Fig. 2A and Fig. S1A). GO analyses (Fig. 2B) of these differential genes identify 52 key genes of three endosymbiotic modules as the top enrichment: (1) Oxidative Phosphorylation (OXPHOS) module includes 22 genes in Complexes I, III, IV, and V; (2) Hemoglobin Synthesis module contains 9 genes involved in heme synthesis within the mitochondria and hemoglobin subunits; and (3) Ribosomal Activity module consists of 21 genes involved in mitochondrial and cytosolic ribosomes (Fig. 2A-B and Fig. S1B-D). This strong and specific enrichment highlights endosymbiotic genes at the transcriptomic frontier of divergence at the early stage of speciation.

Integrating the climate and transcriptomic data, we found that climate conditions of breeding habitats strongly explain the differential transcriptome that is enriched for endosymbiotic interactions (Fig. 2B-H). PC1 of the differential transcriptome among SOCC, STOW and hybrids is positively associated with mean gene expression levels (Fig. S1A) and significantly associated with all three climate variables after controlling for species effect (Fig. 2H, Table S1). In our regression models, both historical and present records of temperature and precipitation effectively explain the differential transcriptome better than species effects (Fig. 2H). Remarkably, the historical VP exhibits a much higher effect size (0.88) than the present VP (0.21) in explaining the transcriptional variation (Fig. 2H). The broad association and temporal specificity indicate transcriptomic adaptation to the historical climate with potential inertia in response to the recent dramatic climate changes.

Beyond the whole transcriptomic patterns, transcription of the three endosymbiotic genetic modules also exhibits signatures of climate adaptation (Fig. 2C-G). The transcription PC1 of endosymbiotic modules, which is positively associated with endosymbiotic gene expression (Fig. S1B-D), shows significant association with historical and present climate variables after controlling for population ancestry. Specifically, PC1 of OXPHOS gene expression is significantly associated with all three climatic variables (Fig. 2C and G). The historical VP has a remarkably greater effect size over the present VP (0.7 vs. 0.26) (Fig. 2C and G; Table S2), reflecting climate niche conservatism (Wiens, J. J., & Graham 2005) in OXPHOS functions. In addition, PC1 of OXPHOS is also significantly associated with the life history morphometric PC1 (effect size = 0.16, $p < 0.05$, Table S2) (Fig. 2D), which is not associated with the other two gene sets ($p > 0.05$). OXPHOS gene-expression patterns are divergent between species, where STOW shows higher expression level (Fig. 2C and Fig. S1C) but lower co-expression level among OXPHOS genes than SOCC (Fig. 2I). Hybrids display intermediate gene expression level (Fig. 2C and Fig. S1C) but the lowest co-expression among OXPHOS genes (Fig. 2I). This OXPHOS-specific phenotypic association elucidates the molecular underpinnings of the observed life history adaptation (Fig. 1J-K) and substantiates the notion that the divergent OXPHOS activities can reflect differential bioenergetics underlying alternative species-specific life history strategies (Tamura et al. 2014; Salgado et al. 2017; Patton et al. 2018).

Ribosomal gene expression also exhibits climate niche conservatism, as its PC1 exhibits stronger association with the historical VP (effect size = 0.47, $p < 10^{-5}$) than with the present VP (effect size = 0.21, $p = 0.006$) (Fig. 2G, Table S3), despite its significant association with all climate variables (Fig. 2G). In addition, the expression of hemoglobin synthesis genes is significantly predicted by the historical (effect size = 0.5, $p < 10^{-5}$) but not the present VP ($p > 0.05$) (Fig. 2F and 2G, Table S4). The repeatedly observed stronger association between historical VP and all three endosymbiotic modules indicates broad climate niche conservatism of endosymbiotic transcription. On the other hand, we also observed adaptive responses to climate change, since endosymbiotic gene expression does track recent precipitation and temperature ($p < 0.05$; Fig. 2G, Table S1). Such adaptive responses are further represented by the higher expression of endosymbiotic genes in STOWs and hybrids than SOCCs (Fig. 2C-F and Fig. S1), indicating heat acclimation of STOWs and hybrids in response to their drier and warmer habitats (Fig. 1G-H).

To sum up, the concordant associations between climatic conditions and transcription of all three endosymbiotic gene modules suggest endosymbiotic climate adaptation (Fig. 2C-G). The equivalent or greater effects of present than historical temperature and precipitation on endosymbiotic transcription (Fig. 2G) suggests

adaptive transcriptional response to climate change. On the other hand, the much greater effect of the historical VP (Fig. 2G) indicates climate niche conservatism of endosymbiotic function, or adaptive inertia in complex climate response.

Bioenergetics Reveals Partial Oxidative Stress in Blood Cells

We characterized bioenergetics of blood samples to determine their metabolic state and any sign of oxidative stress during adaptation. Normal bioenergetics features a negative association between glucose and lipid (**E1**, Randle Cycle) (Randle et al. 1963), reflecting reciprocal inhibition and substrate competition between energy resources (Fig. 3A); a positive correlation between fuel availability and OXPHOS transcription (**E2**) (Fig. 3A) (Bhatti et al. 2017) that reflects harmonized energy metabolism; and a positive correlation between ATP and OXPHOS activity (**E3**) (Fig. 3A) (Kioka, et al. 2014) that represents OXPHOS efficacy. Deviation in any of these features is attributed to cellular stress, which can be further characterized for the relationship between OXPHOS activity and NADPH/$NADP^+$ ratio (Jeon et al. 2012; Lewis et al. 2014. Moon et al. 2020; Schafer, 2019). When OXPHOS operates under oxidative stress (Fig. 3A) (**E'**), the NADPH-dependent antioxidant defense is frequently compromised and leads to a negative association between OXPHOS and NADPH/$NADP^+$ ratio (Jeon et al. 2012; Moon et al. 2020).

We observed the negatively associated FFA and glucose (Randle, 1963) (Fig. 3B) (**E1**) and the positively correlated OXPHOS gene expression with energy resources (glucose and TAG) (Fig. 3B) (**E2**), suggesting features of partially normal metabolism. However, the absence of a positive correlation between OXPHOS transcription and ATP production (**E3**) reflects OXPHOS inefficiency: the expression of NDUFV2 (encoding a core subunit of complex I) is negatively correlated with the ATP level (Fig. 3B) (**E3**), and none of other OXPHOS genes is correlated with ATP ($p > 0.05$). Loss of a positive link between OXPHOS transcription and ATP production suggests disordered OXPHOS biogenesis and/or functions. Such OXPHOS disorders are frequently observed in cells under heat stress (Cao et al. 2023; Larsen et al. 2012), due to asynchronized ribosomal (Sonenberg, N., & Hinnebusch, 2009; Rahaman et al. 2025) and OXPHOS responses to increased temperature (Liu and Brooks, 2012; Salgado et al., 2017; Patton et al., 2018; Sokolova, 2023) that disrupt endosymbiotic synergy for cellular energetics (Sokolova, 2023).

Furthermore, we observed a negative correlation between NADPH/$NADP^+$ ratio and OXPHOS transcription (Fig. 3B) **(E')** that confirms oxidative stress (Jeon et al. 2012; Lewis et al. 2014. Moon et al. 2020; Schafer, 2019). NADPH is consumed for antioxidative protection, sustaining the OXPHOS operation despite metabolic oxidation (Lewis et al. 2014; Moon et al. 2020). In our warbler blood samples, significant negative

correlations are broadly detected between the NADPH/$NADP^+$ ratio and OXPHOS genes involved in the Complexes I, IV and V (Fig. 3B) (**E'**). When cells are under oxidative stress, electron leakage from Complex I incurs a buildup of reactive oxygen species that require antioxidant defense for OXPHOS to further operate at the cost of NADPH (Napolitano, et al. 2021), resulting in a negative correlation between the OXPHOS gene expression level and NADPH/$NADP^+$ ratio.

Integrating metabolic and multiomics data derived from the same blood samples, we identified the strongly climate-associated endosymbiotic transcription behind energetic adaptation to climatic conditions. These molecular insights reflect both climate adaptation (Fig. 2C-H and Fig. 3A, E1-E2) and adaptative inertia that are represented by OXPHOS inefficiency and oxidative stress in the blood cells.

Bioenergetic difference between species

Consistent with the heat acclimation prediction (Keefe et al. 2025), the historically warm-adapted SOCC exhibits the best energy capacity over STOW and hybrids ($p < 0.05$), displaying higher ATP and energy storage in the form of free fatty acid (FFA) and triglyceride (TAG) (Fig. 3C). Moreover, SOCC blood cells have bigger surface areas of the mitochondria inner membrane than STOW (mean difference = 1.01, 95% CI: 0.51 to 1.52, Fig 3D), confirming the stronger SOCC energy capacity (Fig. 3C). These results support the bioenergetic continuity of heat acclimation and heat adaptation (Keefe et al. 2025), with the historically warm-adapted SOCC displaying higher energy capacity and mitochondria inner membrane.

Endosymbiotic co-expression network (ECN) reflects strong molecular synergy

To understand the emergent properties of endosymbiotic bioenergetic activity, we built ECNs for each warbler population (Fig. 4A-C). Molecular synergy between each pair of endosymbiotic genes is identified as a weighted edge of ECN (Fig. 4B). An edge is formed if the absolute transcriptional correlation coefficient of a pair of genes is significantly greater than the transcriptomic background (Fig. 4C). The weight of each edge is the absolute value of the correlation coefficient. The full ECNs in all three warbler populations (Fig. 4C-D) display significantly greater co-expression synergy than randomly sampled equal-sized networks (Fig. 4D, $p < 10^{-15}$). Such transcriptional synergy of endosymbiotic genes is in line with their functional interactions (Sonenberg & Hinnebusch, 2009; Kim et al. 2024; Quirós et al. 2016; Wakigawa, 2025).

Consistent with the heat acclimation prediction and bioenergetics measurements, the historically warm-adapted SOCC has the most synergized and efficient endosymbiotic machinery. SOCC has the highest ECN density that reflects remarkably stronger endosymbiotic synergy over STOW and hybrids ($p < 10^{-15}$) (Fig. 4A-D). Such

synergy facilitates better coordination and efficiency of metabolism that are reflected by the higher energy capacity in SOCC blood cells (Fig. 3C), despite their lower endosymbiotic gene expression than STOW and hybrids ($p < 0.05$) (Fig. 2C-E). The hybrid ECN has significantly fewer edges thus lower synergy than SOCC or STOW ($p < 10^{-15}$), suggesting hybrid incompatibility among mismatched endosymbiotic ancestries as predicted by the Endosymbiotic Snowball Effect (Wang et al. 2025).

The synergy within each of the three endosymbiotic modules (Fig. 4D) is consistent with their known functional interdependence. The Ribosomal Module has the highest synergy over the Hemoglobin Synthesis and OXPHOS Modules (Fig. 4D), reflecting the dependency of mito-ribosomes biogenesis on cyto-ribosomes (Khawaja et al. 2023). The historically warm-adapted SOCC has significantly higher synergy within the Ribosomal and OXPHOS Modules than STOW and hybrids ($p < 10^{-15}$) (Fig. 4D), with hybrids showing the lowest synergy of OXPHOS ($p < 10^{-14}$). This result indicates greater functional integration within OXPHOS and ribosome in the SOCC population. In contrast, STOW has the highest synergy within the Hemoglobin Synthesis Module than SOCC and hybrids ($p < 10^{-15}$), which show similar synergy. The outstanding synergy of Hemoglobin Synthesis module in STOW is reminiscent of high-altitude adaptation, as STOW breeds at significantly higher elevation (Fig. 1A) that requires greater hemoglobin function to strengthen oxygen transport (Storz JF. 2016).

SOCC also displays the highest synergy across functional modules. The Ribosomal Module is the hub (Fig. 4E) of endosymbiotic synergy, as this module tightly synergizes with the Hemoglobin Synthesis and OXPHOS Modules in SOCC ($p < 0.05$) and hybrids ($p < 0.05$) (Fig. 4D-E). Such hub status of the Ribosomal Module (Fig. 4D-E) is consistent with its functions, since mitoribosomes translate the core subunits of OXPHOS, and the biogenesis of mitoribosomes and hemoglobin relies on cytoribosomes (Khawaja et al. 2023). On the other hand, all three modules show similar ($p > 0.05$) hub scores in the ECN of STOW (Fig. 4E). This difference could be related to greater hemoglobin centrality in low-oxygen habitat of STOW (Fig. 1A) where oxygen transportation could be central in the coordination of OXPHOS biogenesis and energy production.

The co-expression synergy between modules is the highest in SOCC, followed by STOW then hybrids (Fig. 4D), suggesting stronger endosymbiotic functional integration in the historically warm-adapted SOCC. Collectively, the species differences in endosymbiotic synergy are consistent with the heat acclimation prediction, where SOCC has the highest endosymbiotic synergy (Fig. 4), bioenergetic efficiency and capacity (Fig. 3).

Introgression across species boundaries reshapes endosymbiotic functions

Since the SOCC ECN has superior synergy and bioenergetic capacity, we hypothesize that the introgression of historically warm-adapted SOCC endosymbiotic variants can be selected by climate change in the hybrid and STOW habitats (Fig. 1G-H). Indeed, our Bayesian Genomic Cline analysis on the whole genome sequencing data confirms the excessive SOCC-biased introgression in endosymbiotic genes (Fig. 5A and D-G), reflected by the significantly negative center (α) and rate (ß) parameters (Fig. 5F-G). Collectively, SOCC endosymbiotic genetic complexes are more efficient and selected to penetrate species boundaries, as they exhibit higher endosymbiotic synergy (Fig. 4D) and total energy capacity (Fig. 3C-D).

On the other hand, hybridization has a negative effect on endosymbiotic adaptation, as genetically discordant hybrids (Fig. 5C) have significantly lower endosymbiotic synergy (Fig. 4) and total energy capacity (Fig. 3C) than parental species. The incompatibility among endosymbiotic genes incurs synergistic selection against hybrids, contributing to speciation (Wang et al. 2025). On the other hand, the synergistic selection of genetic concordance across unlinked genomic regions can be counteracted by gene flow (Felsenstein, 1981). Depending on the tension between synergistic selection and gene flow, adaptive endosymbiotic introgression can penetrate the species boundary when an asymmetric selection favoring the historically warm-adapted SOCC variants is strengthened by climate changes. Remarkably, we uncovered the temporal resolution of these conflicting yet entangled evolutionary forces acting on the endosymbiotic genetic complexes across the species boundary.

Endosymbiotic synergy in response to hybridization & climate change

To understand the effect of climate change and hybridization on endosymbiotic synergy and its implication for bioenergetics and organismal life history, we built a Structural Equation Model (SEM) for Bioenergetic Endosymbiotic Synthesis (BES) with 10,000 simulated ECNs (see Methods) based on our field data (Fig. 1). This comprehensive predicative framework integrates natural genetic recombination, variations in endosymbiotic molecular bioenergetics, and climatic heterogeneity across the allopatric parental range and hybrid zones (Fig. 1 and Fig. 5H-J). BES-SEM reveals alternative endosymbiotic molecular strategies for bioenergetic adaptation to climate change (Fig. 5J; Table S2) that significantly affects life history morphometrics (Fig. 5J, absolute effect size > 0.14, $p < 0.05$).

BES-SEM suggests that the endosymbiotic genetic discordance (Fig. 5H) along with hybridization compromises endosymbiotic synergy (Fig. 5J, effect size = -0.63, $p < 0.05$). The latter in turn significantly and positively (Fig. 5J, effect size = 0.19, $p < 0.05$) predicts the total energy capacity of blood cells (Fig. 5I). Consistently, hybrids display higher genetic discordance among endosymbiotic genes ($p < 0.0001$) than parental

356 species (Fig. 5A-C) with the lowest endosymbiotic synergy (Fig. 4) and blood energetics
357 (Fig. 3). Such integrated results provide direct support to the 'Endosymbiotic Snowball
358 Effect' (Wang et al. 2025), which predicts that the mismatched ancestry in the
359 endosymbiotic genes reduces hybrid fitness. In contrast, the heterozygosity within
360 endosymbiotic genes has an indirect positive effect on endosymbiotic synergy via its
361 significantly negative effect on the latent factor η_3 (Fig. 5J, effect size = -0.4, $p < 0.05$).
362 The latent factor η_3 synthesizes the effects of discordance and heterozygosity, and
363 negatively affects endosymbiotic synergy (Fig. 5J, effect size = -0.63, $p < 0.05$). The
364 positive effect of heterozygosity suggests that the effect of recessive deleterious alleles
365 can be masked in heterozygous state, which maintains endosymbiotic synergy that is
366 simultaneously disrupted by between-loci incompatibility.

367 Furthermore, BES-SEM identifies a negative effect of STOW ancestry on the
368 endosymbiotic synergy that is strongly contextualized in climate change (Fig. 5J).
369 Specifically, the latent variable η_2 positively indicated by STOW ancestry (Fig. 5J, effect
370 size = 0.94, $p < 0.05$) has a significant negative effect on endosymbiotic synergy (Fig.
371 5J, effect size = -0.40, $p < 0.05$). This observation suggests that STOW alleles tend to
372 have recessive deleterious effects on endosymbiotic synergy, considering that the
373 heterozygosity within endosymbiotic genes is positively associated with synergy (Fig.
374 5J). The negative effect of STOW ancestry on endosymbiotic synergy is strongly
375 associated with climate changes (Fig. 5H and J, effect size = 0.82, $p < 0.05$), as the
376 STOW habitats have experienced more dramatic changes than the SOCC habitats (Fig.
377 1G-H). Endosymbiotic synergy could collapse in the face of rapid climate change as the
378 cooperating modules respond with different environmental sensitivity (Sokolova, 2023).

379 In contrast, the blood cells of STOW exhibit an alternative bioenergetic strategy
380 via elevated endosymbiotic transcription as opposed to synergy (Fig. 5J, effect size = -
381 0.18, $p < 0.05$). Like endosymbiotic synergy (see above), elevated endosymbiotic
382 transcription also can promote energy potential of the blood cells (Fig. 5J, effect size =
383 0.18, $p < 0.05$). In particular, the latent variable η_2, which is positively indicated by the
384 STOW ancestry, has a strong positive effect on endosymbiotic transcription (effect size
385 = 0.81, $p < 0.05$). Together, BES-SEM reveals alternative endosymbiotic strategies
386 behind organismal responses to climate change from ancestries adapted to divergent
387 climatic conditions. The alternative adaptive responses can be simultaneously
388 hampered and assisted by hybridization.

389

Discussion

Endosymbiotic synergy and climate adaptation

Our multi-omics, blood cell metabolism, and life history morphometric analyses support the 'Endosymbiotic Bioenergetic Synergy Model', in which the coordinated endosymbiotic activity behind energy metabolism is fundamental to climate adaptation of eukaryotic organisms. In particular, we uncover an endosymbiotic bioenergetic complex that is the most differentially transcribed between the divergently climate-adapted wood warbler species at the early stage of speciation. The transcription levels of these endosymbiotic bioenergetic genes are strongly linked to the breeding climatic conditions after controlling for species effects (Fig. 2). This set of endosymbiotic bioenergetic genes exhibits significant transcription synergy (Fig. 4) that positively predicts blood cell energy capacity (Fig. 3C and Fig. 5J). This synergy is significantly associated with life history morphometrics (Fig. 5J). Collectively, multiple lines of independent evidence converge and suggest the fundamental role of endosymbiotic bioenergetics in organismal climate adaptation.

In response to the dramatic climate changes in the breeding habitats over the recent two decades (Fig. 1), warbler blood cells display signatures of adaptation but also signs of oxidative stress and bioenergetic inefficiency (Fig. 3). Specifically, all breeding habitats experienced higher vapor pressure and temperature with decreased precipitation (Fig. 1). These changes were especially extreme in the habitats of STOW and hybrids (Fig. 1). The latter two populations have significantly inferior bioenergetics (Fig. 3) and endosymbiotic synergy (Fig. 4) than SOCC. Consequently, a less efficient alternative strategy emerged in STOW in the form of elevated antioxidant defense (Fig 3) and endosymbiotic transcription (Fig. 2-3) to maintain bioenergetics (Fig. 5J). In contrast, the historically warm-adapted SOCC strategy with low endosymbiotic transcription (Fig. 2) and high synergy (Fig. 4) appear energetically superior with greater total energy capacity (Fig. 3). The STOW strategy could yet to undergo heat acclimation and evolution towards heat adaptation.

Incompatibility & Introgression

Hybridization acts as a double-edged sword for climate adaptation. On one hand, it leads to endosymbiotic incompatibility (Fig. 5H), which increases endosymbiotic discordance (Fig. 5C), compromises endosymbiotic synergy (Fig. 4), and hampers bioenergetic capacity (Fig. 3C; Fig. 5H and J). On the other hand, hybridization enables the adaptive introgression of the historically warm-adapted SOCC variants (Fig. 5F-G), which could help rescue the STOW population confronting rapid warming (Fig. 5I). Heterozygosity within the endosymbiotic bioenergetic complex indeed promotes

endosymbiotic synergy and bioenergetics despite the negative effect of genomic heterozygosity (Fig. 5J). Remarkably, we observed contrasting effects of hybridization that shape endosymbiotic bioenergetic adaptation across the species boundary of SOCC and STOW.

The future species boundary depends on the tension of adaptive introgression and endosymbiotic incompatibility in the context of climate change. The hybrid zone in Sisters OR may become narrower due to the reduced hybrid fitness that results from the compromised endosymbiotic synergy (Fig. 5F). The hybrid fitness loss can be magnified by the rapidly changing climate in the hybrid habitat (Fig. 1G-H). Simultaneously, the species boundary may shift towards STOW direction as the warm-adapted SOCC endosymbiotic variants asymmetrically penetrate the species boundary (Fig. 5F). Although the adaptive introgression can encounter resistance by the endosymbiotic incompatibility, the SOCC-biased dominance (Fig. 5F) weakens the resistance.

Conclusion

The catastrophic climate changes in the North American temperate rainforest (Fig. 1G) have significant impacts on organismal bioenergetics, life history, and the species boundary. This study unveils the 'Endosymbiotic Bioenergetic Synergy Model' in the forest canopy endotherms by characterizing the highly synergized molecular activities among organelles orchestrating energy metabolism behind climate adaptation. In addition, we observed adaptive inertia especially in populations that have experienced dramatic climate changes, and this inertia can be partially alleviated by the penetration of warm-adapted endosymbiotic genetic variants through the nascent and evolving species boundary.

Materials and Methods

Sampling

We conducted field sampling during the breeding season (June-July) of 2024 by mist-netting with an audio lure (Wang et al. 2019, 2020, De Zwaan et al. 2022) in the breeding territories of SOCC, STOW, and a hybrid zone in Sisters, OR (Fig. 1). Upon capturing each breeding adult, we collected a blood sample then conducted life history morphometric measurements including beak morphology: beak depth, beak width, the distance between the anterior rim of the nares to the tip of the beaks (nares-to-tip), and culmen length, as well as wing chord, the tip of the longest primary to the longest secondary wing feather, tarsus length, and body weight. Meanwhile, blood cells and serum were immediately separated upon collection for storage.

Climate adaptation

To compare the historical versus recent climatic conditions of SOCC, STOW, and hybrid habitats (Fig. 1A), we compared mean temperature (°C), monthly precipitation (mm), and vapor pressure (kPa) of breeding seasons (June and July) of 1970-2000 and 2024, when sampling was conducted in the present study. We acquired the historical climate data from worldclim2 (https://www.worldclim.org/data) (Fick et al. 2017) and the 2024 data from National Aeronautics and Space Administration (NASA) Langley Research Center's Prediction of Worldwide Energy Resources (POWER) Project (https://power.larc.nasa.gov/api/temporal/daily/point) with GPS coordinates of the sampling sites (Fig. 1A-D). To gain yearly average of June-July climate conditions, we downloaded NASA historical climate data of the same variables between 1981-2024. To understand the extent of climate changes along the western forest, we downloaded data of yearly forest cover loss (in hectares) in CA, OR, WA, and ID from Global Forest Watch (https://www.globalforestwatch.org) (Hansen et al. 2013) with the *jsonlite* (Ooms 2014) and *httr* (Wickham 2023) packages in R.

To investigate the three climatic variables in each sampling site, we conducted paired t test. To examine local climatic adaptation of the wood warblers, we conducted correlation tests between the three climatic variables from 1970-2000 and life history morphometrics of breeding adults. In particular, we measured beak shapes: beak depth, beak width, the distance between the anterior rim of the nostril to beak tip (nare.to.tip), and exposed culmen length (Fig. 1K). We also measured body weight, tarsus length, wing chord, the distance between the longest secondary and primary feather (primary.secondary) (Fig. 1K). We conducted reduction of dimensions with centered and scaled principal component analysis (PCA) prior to correlation tests with the climatic variables.

Mitochondrial genetics and protein structure

To understand mitochondrial divergence, we acquired genomic sequences (N = 20 SOCC and N = 20 STOW) of mitochondrial ND2 gene (Krosby & Rohwer 2009) from Genbank (Benson 2013). The sequences were aligned with *msa* function under the *msa* package (Bodenhofer, 2015) in R with the following setting: 'method = "Muscle" (Edgar 2004), gapOpening = 20, gapExtension = 10'. Then, we computed the distance matrix with *dist.ml* with *phangorn* package (Schliep, 2011) in R, to fit an initial neighbor joining tree with *nj* with ape (Schliep, 2019). Then we searched for the maximum likelihood phylogeny under the GTR+G+I model with *pml* function in *phangorn* (Schliep, 2011).

To understand the potential structural difference in the mitochondrial energetic proteins, we downloaded *.pdb* files of ND2 and ATP synthase subunit A from AlphaFold (Varadi et al. 2022). Per-residue root mean square deviation (RMSD) between SOCC and STOW ND2 and ATP synthase subunit A were calculated with ChimeraX-1.11.1 (Pettersen et al. 2021).

Nanopore sequencing of SOCC and STOW reference genomes

Blood cell DNA from adult males was extracted with Blood & Cell Culture DNA Kit (Qiagen), quantified with Qubit dsDNA HS Assay Kit (Thermo Fisher Scientific) and integrity-examined with Genomic DNA HS ScreenTape (Agilent) according to manufacturer's protocols. 1 µg of high-quality gDNA was used to generate libraries with Ligation sequencing DNA V14 kit (Nanopore, SQK-LSK114) that were sequenced ~ 50X on PromethION Flow Cells at Jacobs School of Medicine and Biomedical Sciences of State University of New York, Buffalo.

We assembled SOCC and STOW references using Nanopore sequencing that were annotated with a combination of our RNA-seq data (see below) and the songbird protein homology database. Nanopore reads were trimmed with NanoFilt (-q 10, -l 1000) (De Coster et al. 2018) with adaptors removed by porechop. Then we conducted *de novo* assembly with FLYE (Kolmogorov et al. 2019) and polished the assembly with MEDKA (Oxford Nanopore Technologies. 2018) and model "r94_prom_sup_g507". The polished genome was scaffolded with RagTag (Alonge et al. 2022) and the homologous chromosomes were matched to zebra finch reference (GCF_048771995.1.fa). Non-chromosomal contigs were filtered out with seqkit. Repeats were soft-masked with RepeatModeler 2.0.7 (Flynn et al. 2020). RNA-seq reads were mapped to the repeat-masked genome assembly with HISAT2 (Kim et al. 2019). Annotation was performed by Braker3 (Gabriel et al. 2024) with RNA-seq alignment to the newly assembled genome (--bam) and protein homology database (--prot_seq) of all songbirds. Gene names of

the annotation were extracted with blastp (Camacho et al. 2009) with the following specification: -db uniport and -evalue 1e-5.

The resulting reference genomes are of high quality and continuity: the SOCC assembly has BUSCO = 99.5%, N50 = 73,084,269, L50 = 6; and the STOW assembly has BUSCO = 99.5%, N50 = 73,854,319, L50 = 6.

Whole Genome Sequencing (WGS)

Blood cell DNA was extracted with DNeasy Blood & Tissue Kit (Qiagen, 69504), quantified with Qubit dsDNA HS Assay Kit (Thermo Fisher Scientific) and integrity-examined with Genomic DNA HS ScreenTape (Agilent). 100ng gDNA was used to generate libraries that were sequenced on NovaSeq X (Illumina) by 150 bp paired-end sequencing for 17 SOCC, 10 STOW, and 12 hybrid warblers.

WGS reads were trimmed with trimmomatic-0.39 (Bolger et al. 2014) and aligned to the nanopore genome assembly with bwa (Li et al. 2009). Variant calling was conducted with *bcftools* (Danecek et al. 2021) *mpileup* function with the following specifications: -q 20 -Q 20 -C 50 -Ou. We computed the SNP-based F_{ST} between SOCC and STOW with vcftools (Danecek et al. 2011). To acquire ancestry-informative SNPs, we extracted the genomic positions with $F_{ST} > 0.8$.

Parental species differential gene expression

Blood cell RNA was extracted and quantified with Quant-iT RiboGreen RNA Assay (Thermo Fisher Scientific) according to manufacturer's protocols. RNA integrity was confirmed with High Sensitivity RNA ScreenTape (Agilent), and high-integrity RNA was used to generate RNA-seq libraries. These libraries were sequenced on NovaSeq X (Illumina) by 150 bp paired-end sequencing for 15 SOCC, 9 STOW and 12 hybrid warblers. Differential genes were determined following our previously published procedures with minor modifications (Chen et al. 2021; Chen et al. 2025). Briefly, using cutadapt (Martin, 2011), we performed quality trimming, and poly A and adapter trimming. The trimmed read pairs were mapped with HISAT2 (--sensitive --no-mixed --no-discordant) to the SOCC or STOW reference for high quality alignments, which were counted for exons of annotated genes using featureCounts (strand -s 2) (Yang et al. 2014). DESeq2 package (Love et al. 2014) in R was used to identify differentially expressed genes (FDR<0.05, lfcShrink type=ashr).

Hybrid gene expression and Gene Ontogeny Analysis

To determine heterogeneous ancestry representation in hybrid transcriptomes, we generated individual-specific mosaic parental reference to quantify hybrid gene expression. In particular, we aligned the RNA-seq and WGS reads from each hybrid

individual to both parental reference genomes, using HISAT2 and bwa. For each gene region (with 1Kb flanking around the start and end of the gene), we calculated its sequence alignment scores to both STOW and SOCC reference with the WGS data from each of the same sample. We then used the reference of the higher score to quantify gene expression counts. This WGS-guided gene-specific reference provides independent ancestry information for hybrid RNA-seq alignment and quantification, which were further processed following the same procedure as parental species above.

Gene Ontogeny analysis on the divergently expressed genes between the parental species was conducted with goProfiler (Raudvere et al. 2019) and *tguttata* genes network. We extracted the genes corresponding to the significant GO terms for downstream analyses.

Climatic adaptation in metabolic transcription

To understand transcriptive adaptation to climatic conditions, we examined the climate association with gene expression in the enriched molecular clusters (OXPHOS, Ribosomal, and Hemoglobin Synthesis Pathways). We first conducted reduction of dimensions with centered and scaled principal component analyses of the gene expression profiles of each genetic cluster. Then we conducted regression modeling in which the response variables were PC1 of differential transcriptome, and the predicting variables were species (SOCC, STOW, vs hybrids), historical (1970-2000) and present (2024) climate (temperature, precipitation, and vapor pressure). We examined the association between mean gene expression level and transcription PC1 with a linear regression to determine the transcription orientation of the PC1. To accurately and effectively represent the climatic condition of each bird's breeding habitat, we extracted the June-July air temperature (C°) at 2 meters above the Earth's surface, monthly precipitation (mm), and vapor pressure (kPa) at the GPS coordinate where each sample was collected. We fitted a regression model for each climate variable to compare the effects of historical versus present climatic conditions while controlling for species effect. To understand the range of effects of each historical and present climate variables, we conducted 1000 bootstrap sampling of the full dataset to generate the bootstrap distribution of effect size for each climate variable.

Endosymbiotic Co-expression Network (ECN)

To examine the synergy among endosymbiotic genes, we constructed a co-expression network among genes in the three endosymbiotic modules (see **Gene Ontogeny Analysis**) in each population (SOCC, STOW, or hybrid). Each node represents a gene. An edge emerges if the pair of genes are significantly co-expressed in each population. The edge weight is the absolute co-expression correlation

coefficient between the two genes in the designated population. The 95th percentile of the absolute correlation coefficients of all pairwise co-expressions in the transcriptome was used as the threshold for significant co-expression. If the expression correlation coefficient between a pair of genes was greater than that threshold in a population, an edge would form between this pair of gene nodes. The weight of the edge is the absolute value of the correlation coefficient. All pairwise co-expression associations of the 52 genes from the three functional modules (see above) were evaluated to generate the full Endosymbiotic Co-expression Network (ECN) of each population.

To determine the synergy among endosymbiotic genes in each population, we quantified edge density (Wasserman, 1994) and global efficiency (Vragović, 2005) of each ECN with *igraph* (Csardi & Nepusz. 2006) in R. Furthermore, we evaluated the synergy within each functional module and sub-module. For each network, module, or sub-module of a population (SOCC, STOW, or hybrid), we randomly generated 10,000 subsamples consisting ¾ of the nodes. To test whether the ECN was significantly different from random co-expression, we generated a null distribution by randomly sampling 10,000 equal-sized co-expression networks from the transcriptome. We then conducted one-way ANOVA followed by *post hoc* tests with Bonferroni multiple hypotheses correction (Bonferroni 1936) to compare endosymbiotic synergy of ECNs among different populations relative to the null distribution.

To understand the relative centrality of the three functional modules, we calculated the mean weighted centrality hub score (Kleinberg, 1997) of vertices within each module. The module with greatest the hub score is the central connector of ECN.

Hybrid genomics and endosymbiotic genetics

The genomic ancestry of each individual is calculated with ancestry informative SNPs ($F_{ST} > 0.8$ between SOCC and STOW) (Wang et al. 2021). SNP-calling was conducted with bcftools (Danecek et al. 2021). F_{ST} was calculated with vcftools (Danecek et al. 2011) excluding sites with low quality scores and depth (QUAL < 20, DP <10) or missing > 30% data. Homozygous SOCC, heterozygous and STOW genotypes were represented with scores 0, 0.5, and 1, respectively. Genomic hybrid index (HI) for each individual is the average of all the ancestry-informative SNPs. Divergent endosymbiotic genetic positions were extracted as SNPs within the 53 divergently expressing endosymbiotic genes (see **Gene Ontogeny Analysis section**) with maximum missing genotype being 30% across all individuals, with the mean HI difference of at least 0.3 between SOCC and STOW. The standard deviation of HI across the divergent endosymbiotic genetic positions provides a proxy of 'endosymbiotic genetic discordance' (EGD). We tested whether EGD was significantly different between SOCC, STOW, and hybrids with ANOVA followed by TukeyHSD *post*

hoc tests. In addition, we estimated individual heterozygosity both for the ancestry-informative as well as for the endosymbiotic genetic positions. Heterozygosity is calculated as the fraction of heterozygous sites of total sites.

To understand the introgression of endosymbiotic genes relative to the genomic background, we conducted Bayesian genomic cline analyses (Gompert & Buerkle 2011). Specifically, we examined the deviation of endosymbiotic genetic HI from genomic HI, by estimating two parameters: α and ß that represent the direction and the rate of introgression, respectively. While 0 values of α and ß represent neutral diffusion, a significantly positive vs negative $\alpha(s)$ reflect STOW vs SOCC-biased introgression. A significantly positive ß implies divergent selection, whereas a significantly negative ß represents excessive introgression.

Blood cell bioenergetics

To evaluate the bioenergetic conditions of blood cells, we integrated transcriptomics with energy metabolism analyses. We examined three expectations of normal bioenergetics: (E1) signature of Randle Cycle, which expects a negative correlation of glucose level and Triglyceride (TAG); (E2) fuel availability whether through glycolysis versus lipolysis should be positively associated with OXPHOS activity; (E3) OXPHOS efficiency, reflected as the relationship of OXPHOS gene expression and ATP output. Cell stress is indicated if one or more of E1-E3 was rejected. If so, we evaluated prediction of oxidative stress (E') as indicated by the association of NADPH/$NADP^+$ ratio and OXPHOS gene expression. Under oxidative stress, the electron transport chain activity leads to ROS leakage, and more antioxidant defense and NADPH consumption, resulting in a negative association of NADPH/$NADP^+$ ratio and OXPHOS activity.

To investigate the four bioenergetic expectations (E1-E', Fig. 3), we quantified the following metabolites: (1) glucose levels, (2) TAG, (3) FFA, (4) ATP, and (5) NADPH/NADP+ ratio in blood cells of for 5 SOCC, 6 STOW and 11 hybrid breeding warblers. The association analyses between blood biochemical profiles and OXPHOS gene expression were performed using the same blood samples.

To compare the energetics among species, we derived the metric of 'Total Energy Potential', which is the weighted average of scaled ATP production and energy source. The energy source is approximated as the weighted average of glucose, FFA, and TAG in the ratio of 1: 3.5: 11, reflecting the ATP production capacity.

Immunochemistry, imaging and quantification

The crosslinked, snap-frozen blood cells were used for immunochemistry following a published protocol (Chen et al., 2025) with a COX IV primary antibody

(ab16056) at 1:500 and secondary antibodies (Thermo Fisher Scientific) at 1:1,000 to visualize the mitochondria inner membrane. DAPI was used as a counterstain of nuclei. Confocal images of separate single cells were taken for maximum-intensity z-series projections, and the total mitochondria inner membrane area was quantified using the in FIJI for each cell. The mitochondria inner membrane area of each animal was calculated as the average of thirty randomly imaged blood cells for each of the three biological replicates. Statistical significance was determined by nested Bootstraping tests.

Climate change scores

We computed the climatic deviation (**δ**) among three climate variables, where the deviation for each climate variable is the difference between 2024 and 1970-2000 average. For instance:

$$\delta_{prec} = prec_{2024} - prec_{1970-2000}$$

To evaluate the effect of climate change, we transformed the climate deviation score into the Scaled Climate Change Score (***p***), which is the subsample average of δ_i for each time, and the location is scaled relative to the all-time maximum (δ_{max}) and minimum (δ_{min}) change of the respective climate variable:

$$\boldsymbol{p} = \frac{\delta_i - \delta_{min}}{\delta_{max} - \delta_{min}}$$

The Scaled Climate Change Scores for temperature, precipitation, and vapor pressure are respectively denoted as p_T, p_P, and p_V.

Simulated endosymbiotic synergetic evolution

To understand the evolution of endosymbiotic synergy in bioenergetic responses to climate change and hybridization, we simulated 10,000 ECNs in an integrative predictive framework (see below). To best leverage the natural variation among SOCC, STOW, and hybrids, we mixed the samples from all three populations to form a virtual panmictic population. In each iteration, we randomly sampled 16 out of 39 individuals from the virtual panmictic population to compute an ECN. We estimated the endosymbiotic synergy as the global efficiency of the ECN. Simultaneously, for each ECN, we recorded the corresponding average scaled climate change scores, genomic hybrid index, genomic heterozygosity, endosymbiotic genetic discordance, as well as the hybrid index and heterozygosity of endosymbiotic genes (see Genomic Hybrid Index and Endosymbiotic Genetic Discordance). In addition, we recorded the blood total energy potential and life history morphometrics.

Bioenergetic Endosymbiotic Synthesis Structural Equation Model (BES-SEM)

To predict the effect of climate change and hybridization on blood cell energetics and life history morphometrics, we built a structural equation model (SEM) for a bioenergetic endosymbiotic synthesis (BES). The BES-SEM has a measurement model with three latent variables, and a structural model with three layers: (1) a molecular mediator layer, (2) an energetic mediator layer, and (3) the life history outcome layer. The three latent variables (η_1, η_2, η_3) are respectively indicated with a set of measurement variables. Specifically, η_1 reflects climate changes, and is presented by scaled climate scores for temperature (p_T), precipitation (p_P), and vapor pressure (p_V); η_2 represents genetic ancestry, indicated by the genomic hybrid index and the hybrid index of endosymbiotic genes; η_3 represents genetic discordance, synthesizing genomic heterozygosity, heterozygosity of endosymbiotic genes, and genetic discordance within endosymbiotic genes. The latent variables are then linked to the molecular mediator layer with (1) PC1 of endosymbiotic gene expression level; (2) endosymbiotic synergy measured by the global efficiency of ECNs (see ECN section). The molecular mediator layer then predicts the energetic mediator layer with total energy capacity (see Blood Cell Bioenergetics section). The mediator layer further predicts the outcome layer with the PC1 and PC2 of life history morphometrics. Across layers, the indirect effects from each latent variable to each mediator and outcome variable are incorporated. The BES-SEM is constructed with *lavaan* package (Rosseel et al. 2012) in R. The full hierarchical SEM is estimated with maximum likelihood. The 95% confidence intervals for each indirect effect are computed with bias-corrected and accelerated bootstrap resampling with 1,000 replications.

Competing Interest

We declare no competing interest.

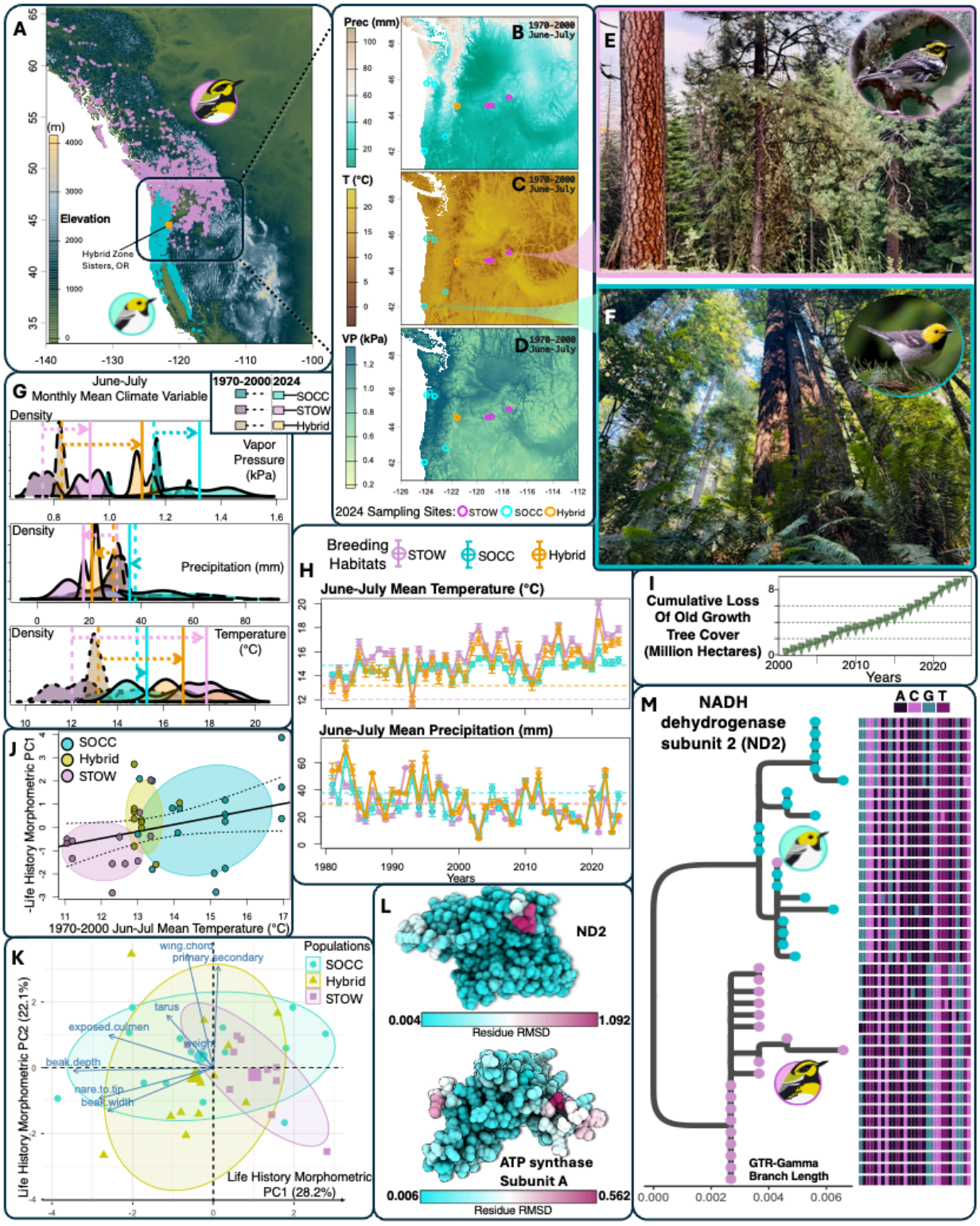

Fig. 1 Climatic gradient of the wood warbler breeding habitats and signatures of local climatic adaptation. (A) The breeding range of SOCC and STOW with elevation presented in meters. **(B-D)** Sampling locations of this study are labeled over the

historical climatic baseline (June-July, 1970-2000) for monthly precipitation (Prec), mean temperature (T) and vapor pressure (VP). **(E-F)** Breeding habitat photos of SOCC (E) and STOW (F) by Silu Wang. SOCC and STOW portraits by Frode Jacobsen and Silu Wang, respectively. **(G)** Current breeding habitats are significantly warmer and dryer than they were in 1970-2000. Arrows indicate the direction of changes in precipitation, temperature, and vapor pressure. **(H)** Yearly changes of the average June-July temperature (top) and precipitation (bottom) between 1980 and 2023 at the sampling sites of this study. **(I)** Loss of old-growth tree coverage between 2000 and 2023 in forests of WA, OR, ID, and CA, USA. **(J)** PC1 of life history morphometrics is significantly correlated with the historical breeding season temperature. Dots represent individual warbler samples. **(K)** PCA of life history morphometrics of breeding adults. PC1 reflects beak shape and PC2 represents wing size. **(L)** Sequence-based modeling predicts divergent 3D protein structures of NADH dehydrogenase subunit 2 (ND2) and ATP synthase subunit A between SOCC and STOW. The magenta components are residues with high dissimilarity between SOCC and STOW in per-residue root mean square deviation (RMSD). **(M)** SOCC and STOW harbor distinct mitochondrial ancestries within the ND2 gene that were previously shown to covary with climatic conditions in ancient hybrid populations (Wang et al. 2021). Maximum likelihood gene tree of ND2 with nucleotide alignment of top 30 most divergent substitutions suggests near-reciprocal-monophyly.

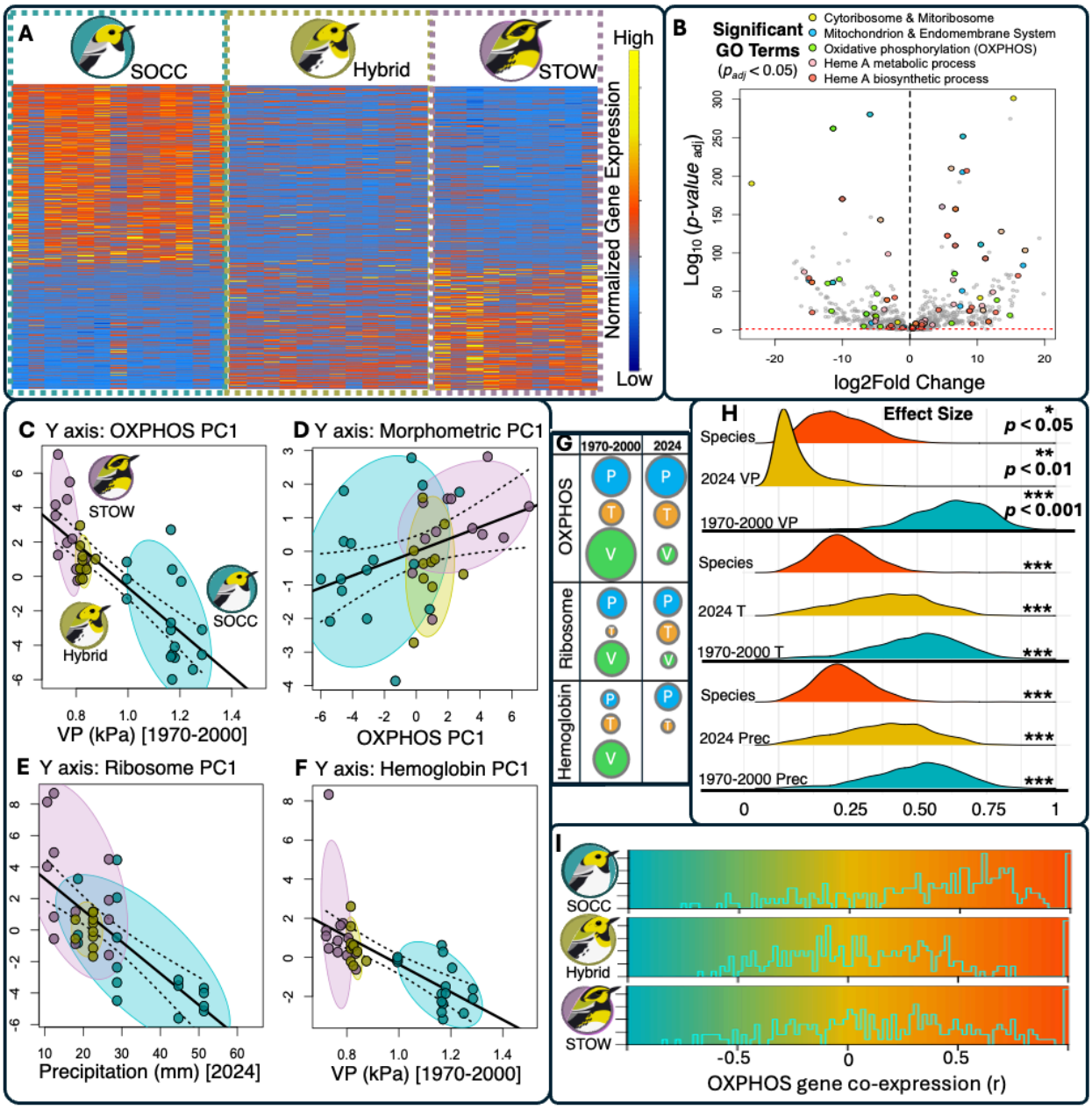
A
SOCC
Hybrid
STOW
High
Normalized Gene Expression
Low
B
Significant GO Terms (p_{adj} < 0.05)
Cytoribosome & Mitoribosome
Mitochondrion & Endomembrane System
Oxidative phosphorylation (OXPHOS)
Heme A metabolic process
Heme A biosynthetic process
Log10 (p-value adj)
log2Fold Change
C Y axis: OXPHOS PC1
VP (kPa) [1970-2000]
D Y axis: Morphometric PC1
OXPHOS PC1
E Y axis: Ribosome PC1
Precipitation (mm) [2024]
F Y axis: Hemoglobin PC1
VP (kPa) [1970-2000]
G
1970-2000
2024
OXPHOS
Ribosome
Hemoglobin
H
Effect Size
Species
2024 VP
1970-2000 VP
2024 T
1970-2000 T
2024 Prec
1970-2000 Prec
p < 0.05
p < 0.01
p < 0.001
I
SOCC
Hybrid
STOW
OXPHOS gene co-expression (r)

Fig. 2 Endosymbiotic transcriptional divergence and climate adaptation. (A) Genes of differential expression (N = 2,037) between SOCC (turquoise box) and STOW (magenta box) display intermediate expression in hybrids (yellow box). **(B)** The differential genes are most enriched for factors involved in the endosymbotic bioenegetic cooperation among mitochondria, ribosomes, and nucleus. **(C-D)** Transcription PC1 of differential genes involved in OXPHOS is significantly ($p < 0.05$) associated with the historical vapor pressure (C) and the PC1 of life history morphometrics (D). **(E)** Transcription PC1 of differentially expressed mitoribosomal and cytoribosomal genes are negatively assocaited ($p < 0.05$) with the precipitation in 2024. **(F)** Transcription PC1 of differential genes involved in Hemoglobin Synthesis is negatively associated with VP in 1970-2000, but not with VP in 2024. **(G)** Relative effect sizes of the associations between climate variables (P, precipitation; T, temperature; V, vapor pressure) and the transcription PC1 of differential genes involved in (1) OXPHOS, (2) Ribosomal, and (3) Hemoglobin Synthesis. Both historical and present climate variables are incorperated in the same model that predicts each transcription PC1. Circles represent statistically significant effects of the corresponding climate variables. Circle size is proportional to the effect size. All these analyses in C-G have controlled for species effect. **(H)** Bootstrap distributions of effect sizes of three regression models that predict the PC1 of the differential genes by climate and species variables. The climate predictors are vapor pressure (VP), temperature (T), and precipitation (Prec). Both historical and present climate variables significantly explain the transcription PC1 of differential genes after controlling for species effect. Historical climatic variables (blue) have larger effect sizes than the 2024 counterparts (yellow). **(C-H)** Transcription PC1s are positively associated with mean transcription levels of each individual (Fig. S1). **(I)** Density distribution of co-expression coefficients among OXPHOS genes. High frequencies of positive coexpression are observed in SOCC but not STOW or hybrids.

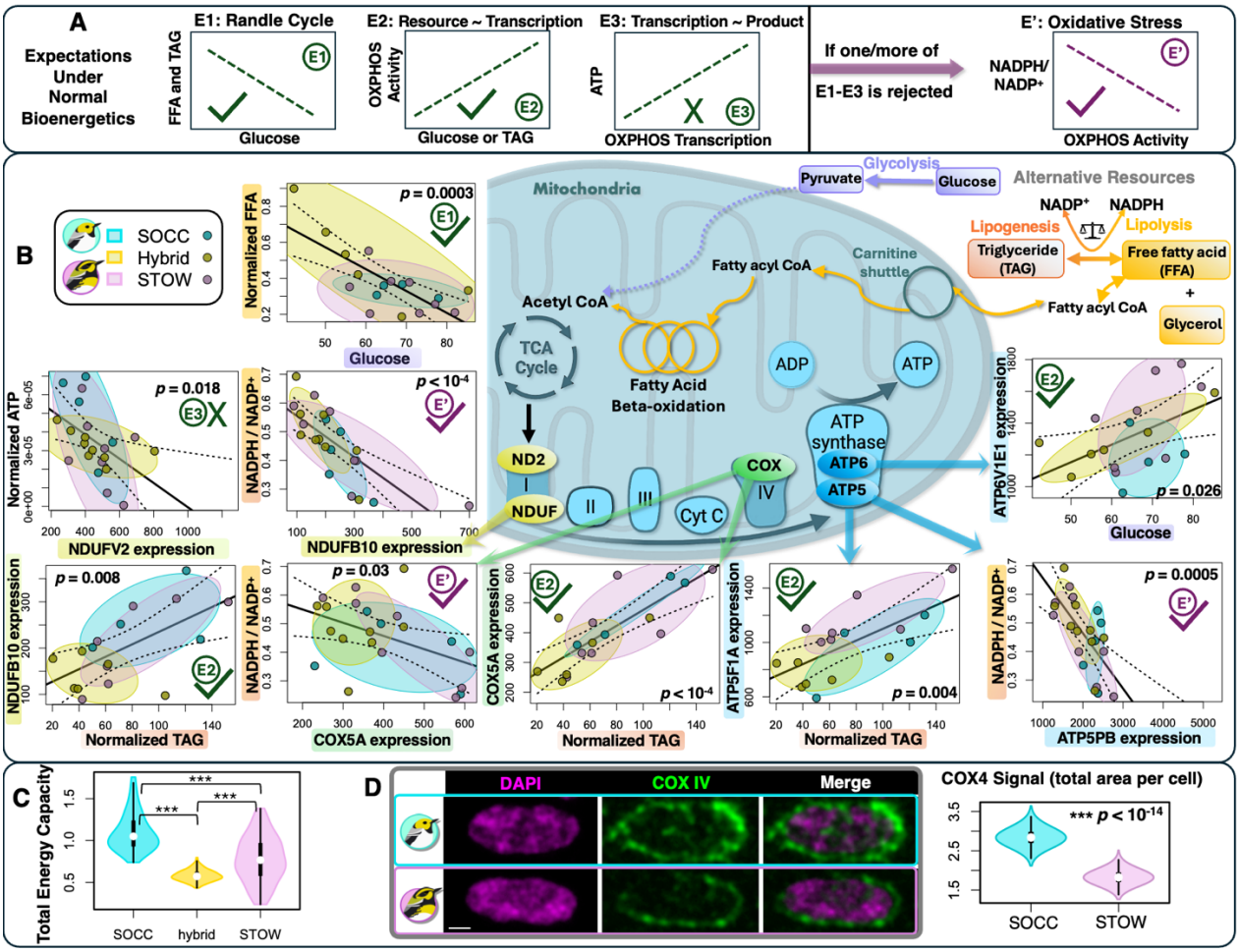
A
Expectations Under Normal Bioenergetics
E1: Randle Cycle
FFA and TAG
Glucose
E2: Resource ~ Transcription
OXPHOS Activity
Glucose or TAG
E3: Transcription ~ Product
ATP
OXPHOS Transcription
If one/more of E1-E3 is rejected
E': Oxidative Stress
NADPH/ NADP+
OXPHOS Activity
B
SOCC
Hybrid
STOW
Mitochondria
Glycolysis
Pyruvate
Glucose
Alternative Resources
NADP+
NADPH
Lipogenesis
Lipolysis
Triglyceride (TAG)
Free fatty acid (FFA)
Glycerol
Fatty acyl CoA
Carnitine shuttle
Acetyl CoA
TCA Cycle
Fatty Acid Beta-oxidation
ADP
ATP
ATP synthase
ATP6
ATP5
ND2
NDUF
II
III
Cyt C
COX
IV
Normalized FFA
p = 0.0003
Glucose
Normalized ATP
p = 0.018
NDUFV2 expression
NADPH / NADP+
p < 10-4
NDUFB10 expression
ATP6V1E1 expression
p = 0.026
NDUFB10 expression
p = 0.008
Normalized TAG
p = 0.03
COX5A expression
COX5A expression
p < 10-4
Normalized TAG
ATP5F1A expression
p = 0.004
Normalized TAG
p = 0.0005
ATP5PB expression
C
Total Energy Capacity
SOCC
hybrid
STOW
D
DAPI
COX IV
Merge
COX4 Signal (total area per cell)
*** p < 10-14
SOCC
STOW

775

Fig. 3 Endosymbiotic bioenergetics of the warbler blood cells sampled in the 2024 breeding season. (A) Expected features of normal (E1-E3) or stressed (E') metabolism that are confirmed (checkmarks) or contradicted (crossed, E3) by metabolite quantification of blood cells in this study. **E1**, Randle Cycle, where alternative fuel sources negatively associate during healthy cell metabolism. **E2**, normal OXPHOS expression positively associates with energy source. **E3**, OXPHOS expression normally positively predicts the ATP level. **E'**, a negative correlation between OXPHOS expression and $NADPH/NADP^+$ ratio indicates oxidative stress. **(B)** Quantification of metabolites and transcriptomics confirms E1 and E2 but contradicts E3, suggesting metabolism under a stressed state that is further confirmed by E'. The validated **E1**: a negative association of glucose and FFA (top left, $p < 0.05$) supports the Randle Cycle, featuring the competing glycolysis (purple) versus lipolysis (orange) as alternative energy sources. The validated **E2**: expression of various OXPHOS genes collectively and positively correlates with energy sources, glucose and TAG, fulfilling energy demand via enhanced metabolism. The contradicted **E3**: disordered OXPHOS function is detected as ATP abundance is not positively correlated with OXPHOS gene expression. The validated **E'**: oxidative stress is suggested by the negative correlation between $NADPH/NADP^+$ ratio and OXPHOS gene expression ($p < 0.05$), indicating the depleted NADPH reserve for antioxidant defense. **(C)** ATP and resource substrate quantification indicates that SOCC (bootstrap 95% CI: 0.81-1.69) has significantly higher total energy capacity than STOW (bootstrap 95% CI: 0.28-1.29), which surpasses hybrids (bootstrap 95% CI: 0.47-0.72). **(D)** Confocal imaging visualizes the mitochondrial inner membrane (anti-COX IV) and nuclei (DAPI) of blood cells and elucidates a significantly larger mitochondrial inner membrane area per blood cell in SOCC than STOW ($p < 0.05$). Scale bar: 1 μm. Three biological replicates per species.

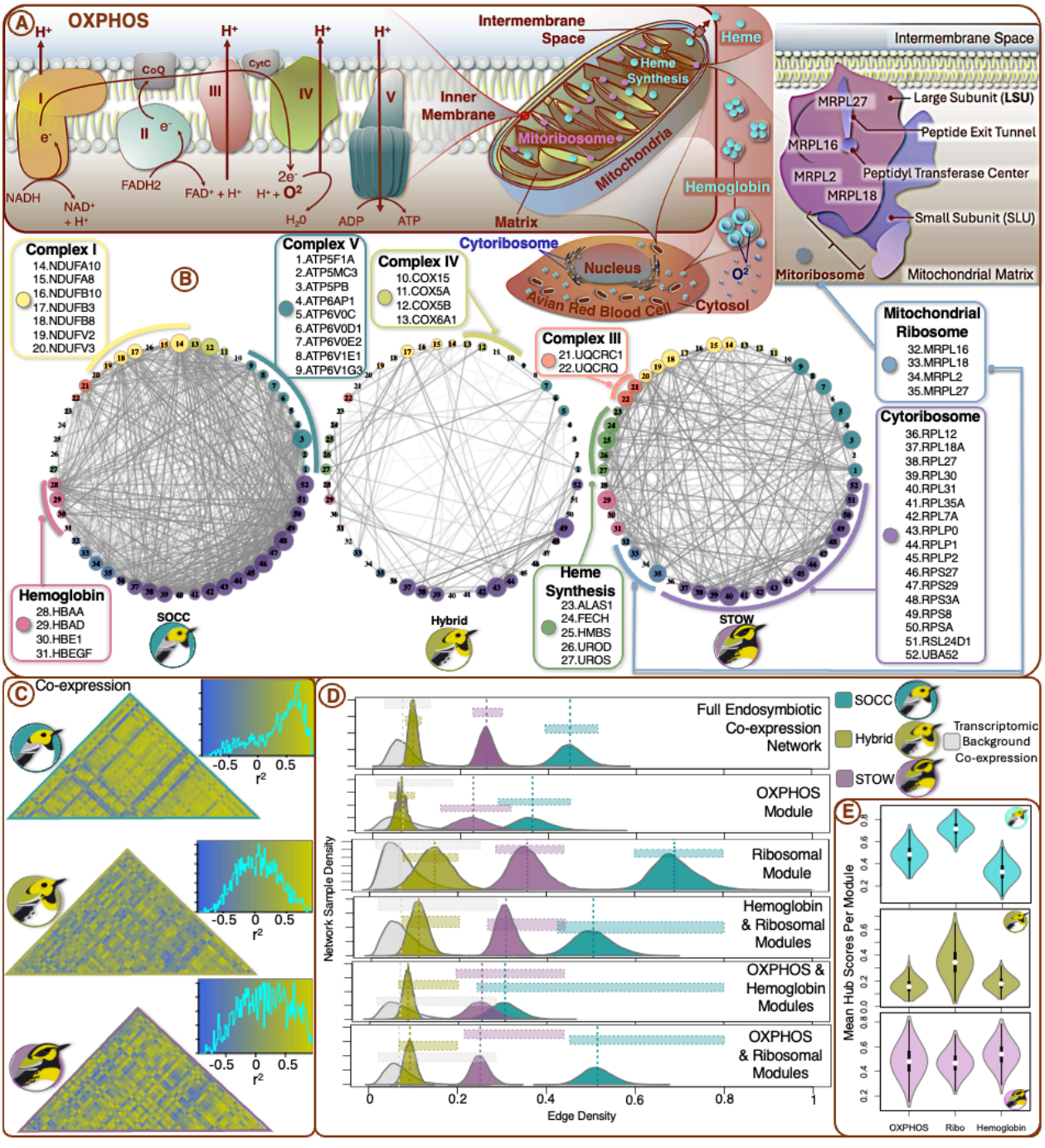
A
OXPHOS
Intermembrane Space
Inner Membrane
Matrix
Heme
Heme Synthesis
Mitoribosome
Mitochondria
Hemoglobin
Intermembrane Space
MRPL27
Large Subunit (LSU)
Peptide Exit Tunnel
MRPL16
MRPL2
Peptidyl Transferase Center
MRPL18
Small Subunit (SLU)
Mitoribosome
Mitochondrial Matrix
Cytoribosome
Nucleus
Avian Red Blood Cell
Cytosol
B
Complex I
14.NDUFA10
15.NDUFA8
16.NDUFB10
17.NDUFB3
18.NDUFB8
19.NDUFV2
20.NDUFV3
Complex V
1.ATP5F1A
2.ATP5MC3
3.ATP5PB
4.ATP6AP1
5.ATP6V0C
6.ATP6V0D1
7.ATP6V0E2
8.ATP6V1E1
9.ATP6V1G3
Complex IV
10.COX15
11.COX5A
12.COX5B
13.COX6A1
Complex III
21.UQCRC1
22.UQCRQ
Mitochondrial Ribosome
32.MRPL16
33.MRPL18
34.MRPL2
35.MRPL27
Cytoribosome
36.RPL12
37.RPL18A
38.RPL27
39.RPL30
40.RPL31
41.RPL35A
42.RPL7A
43.RPLP0
44.RPLP1
45.RPLP2
46.RPS27
47.RPS29
48.RPS3A
49.RPS8
50.RPSA
51.RSL24D1
52.UBA52
Hemoglobin
28.HBAA
29.HBAD
30.HBE1
31.HBEGF
Heme Synthesis
23.ALAS1
24.FECH
25.HMBS
26.UROD
27.UROS
SOCC
Hybrid
STOW
C
Co-expression
r²
D
Full Endosymbiotic Co-expression Network
OXPHOS Module
Ribosomal Module
Hemoglobin & Ribosomal Modules
OXPHOS & Hemoglobin Modules
OXPHOS & Ribosomal Modules
Network Sample Density
Edge Density
SOCC
Hybrid
STOW
Transcriptomic Background Co-expression
E
Mean Hub Scores Per Module
OXPHOS
Ribo
Hemoglobin

801

Fig. 4 Endosymbiotic Co-expression Networks, ECN. (A) Demonstration of endosymbiotic functions in avian red blood cells, featuring cytoribosome, mitoribosome, hemoglobin synthesis, as well as OXPHOS proteins involved in electron transport chain (Complex I-IV) and ATP synthase (Complex V). The core subunits of OXPHOS proteins (complexes I-V) are translated in mitoribosomes, and utilize oxygen delivered by hemoglobin to generate ATP. These key components are highly enriched among genes of differential expression between SOCC and STOW (Fig. 2 B). **(B)** Endosymbiotic Coexpression Networks of SOCC, hybrids, and STOW. Each node represents an endosymbiotic gene, which shares the same color to its encoded functional protein in panel A. Each edge (line) connecting two genes represents a significant coexpression relationship, with the line darkness in proportion to its weight (absolute value of pairwise correlation coeffcient r^2). The node size represents its strength, which is the weight sum of all its edge connections. Each endosymbiotic coexpression network consists of three main functional modules (1) OXPHOS-encoded components of Complexes I, III, IV, V in yellow, orange, light blue, and light green, respectively; (2) hemoglobin genes involved in heme-synthesis (dark green) and hemoglobin subunits (pink); and (3) ribosome components that include mitoribosomal (dark blue) and cytoribosomal (purple) factors. **(C)** Heatmaps showing pairwise correlation coeffcients (r^2) among the transcription levels of endosymbiotic genes in SOCC, hybrids and STOW. SOCC shows higher frequencies of strong positive co-expression than STOW and hybrids. **(D)** The edge density within each network or module class reflects coexpression strength as a proxy of the synergy among endosymbiotic genes. The SOCC network (turquoise) exhibits much higher endosymbiotic synergy than STOW (magenta) and hybrids (gold) in the full network (top), within the OXPHOS module, within the ribosomal module, and among modules. The 95% CI of each distribution is represented by the horizontal rectangles above the corresponding density curve. **(E)** The bootstrap mean of hub centrality across OXPHOS, Ribosomal, and Hemoglobin Modules.

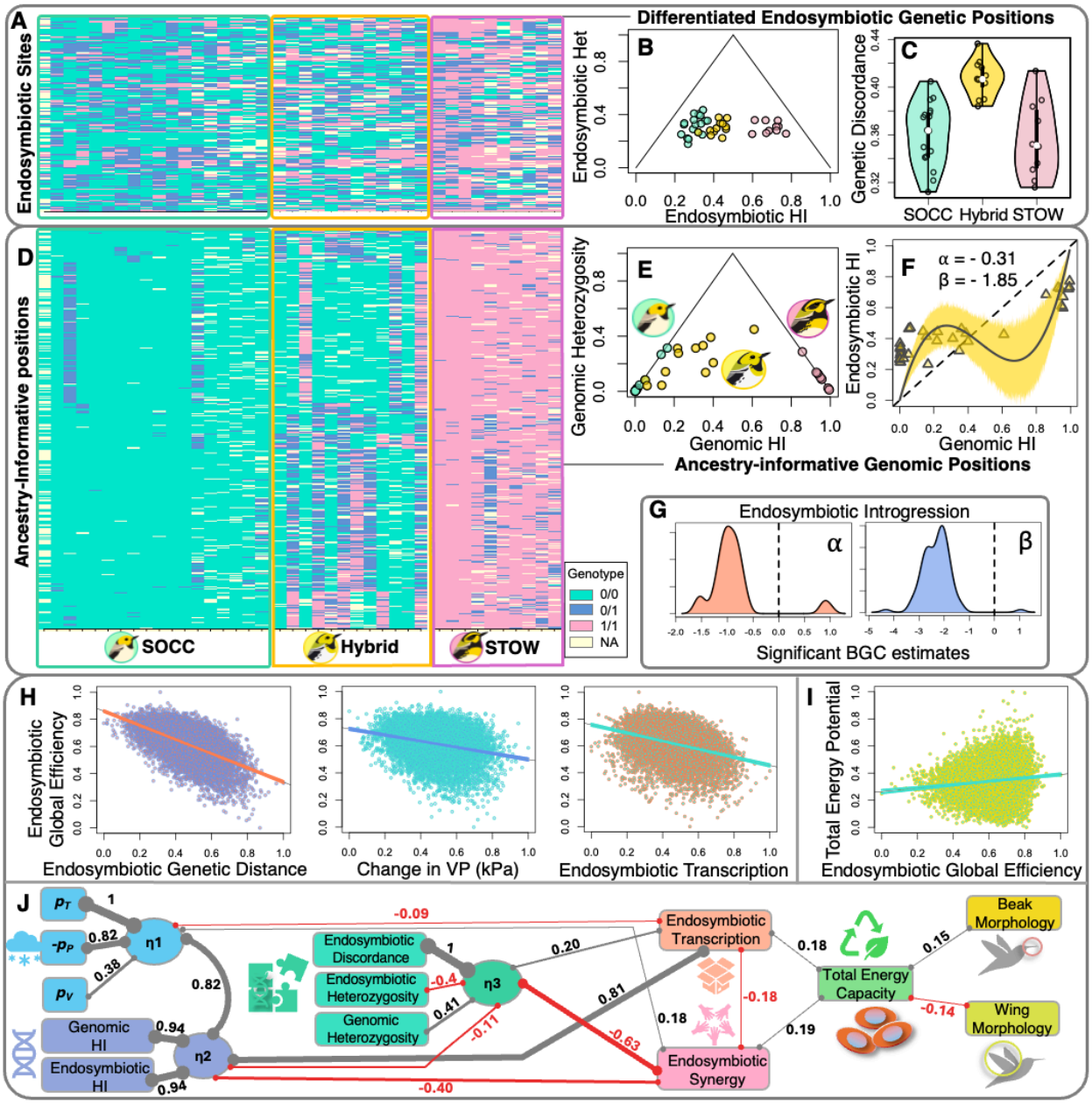
A
Endosymbiotic Sites
Differentiated Endosymbiotic Genetic Positions
B
Endosymbiotic Het
Endosymbiotic HI
C
Genetic Discordance
SOCC Hybrid STOW
D
Ancestry-Informative positions
SOCC
Hybrid
STOW
Genotype
0/0
0/1
1/1
NA
E
Genomic Heterozygosity
Genomic HI
F
α = - 0.31
β = - 1.85
Endosymbiotic HI
Genomic HI
Ancestry-informative Genomic Positions
G
Endosymbiotic Introgression
α
β
Significant BGC estimates
H
Endosymbiotic Global Efficiency
Endosymbiotic Genetic Distance
Change in VP (kPa)
Endosymbiotic Transcription
I
Total Energy Potential
Endosymbiotic Global Efficiency
J
Endosymbiotic Discordance
Endosymbiotic Heterozygosity
Genomic Heterozygosity
Genomic HI
Endosymbiotic HI
η1
η2
η3
Endosymbiotic Transcription
Endosymbiotic Synergy
Total Energy Capacity
Beak Morphology
Wing Morphology

829

Fig. 5 Endosymbiotic Synergy in response to climate change and introgression across the wood warbler species boundary. (A) Genotypes of divergent genetic positions within the endosymbiotic genes. **(B)** Triangle plot characterizing genetic hybrid index (HI) and heterozygosity of reflects admixture patterns within endosymbiotic genes. Each dot represents one warbler. **(C)** Hybrids display significantly more genetic discordance than the parental species ($p < 0.05$). **(D)** Genotypes of ancestry-informative positions across the genome in SOCC, STOW, and hybrids. Each column represents one warbler. **(E)** Triangle plot showing the genomic HI and heterozygosity across SOCC (turquoise), STOW (magenta), and hybrids (gold). **(F)** Bayesian Genomic Cline (BGC) analysis characterizing the deviation of ancestry within endosymbiotic genes relative to the genomic background in hybrids and parental species. BGC reveals excessive SOCC-biased introgression in endosymbiotic genes. **(G)** Distribution of the significant ($p < 0.05$) BGC estimates of introgression direction (α) and rate ($ß$) across endosymbiotic genes are predominantly negative, consistent with the excessive SOCC-biased introgression. **(H)** The simulated networks generated with random samples from the panmictic population (with SOCC, STOW, and hybrids) reveal that endosymbiotic molecular synergy represented by the global efficiency of the endosymbiotic co-expression network is significantly ($p < 0.05$) and negatively predicted by the genetic discordance of endosymbiotic genes, the changes in vapor pressure between 1970-2000 and 2024, and the transcription level of endosymbiotic genes. **(I)** Endosymbiotic synergy in the networks sampled from the simulated panmictic population positively predicts total energy capacity (ATP and resource quantity) of the blood cells. **(J)** Bioenergetic Endosymbiotic Synthesis Structural Equation Model (BES-SEM). To predict organismal responses to climate change, BES-SEM integrates the effects of climate change, transcriptomics, genomic composition by hybridization, blood bioenergetics, and life history morphometrics. The positive versus negative relationships is represented by grey and red lines, respectively, with the effect sizes of significant relationships above the paths. Line thickness represents effect size.

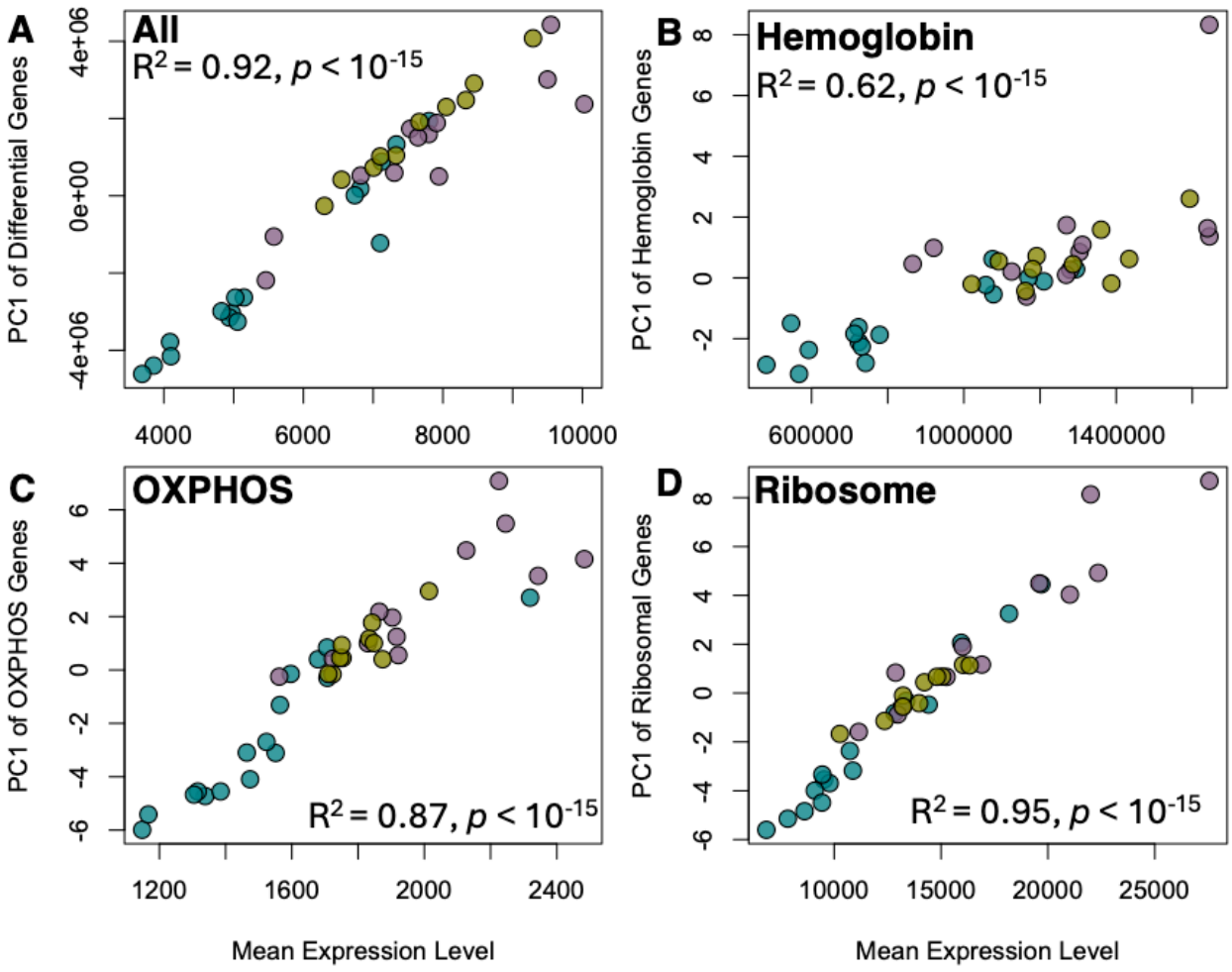

858

859 **Fig.S1 The positive associations between transcription PC1 and gene expression**
860 **levels** of **(A)** all 2,037 differential genes, **(B)** Hemoglobin synthesis genes, **(C)**
861 OXPHOS genes, and **(D)** Ribosomal genes. Turquoise, SOCC; yellow, hybrids;
862 magenta, STOW. Each dot represents one warbler.

Reference

Alonge, M., L. Lebeigle, M. Kirsche, K. Jenike, S. Ou, S. Aganezov, X. Wang, Z. B. Lippman, M. C. Schatz, and S. Soyk. 2022. Automated assembly scaffolding using RagTag elevates a new tomato system for high-throughput genome editing. Genome Biol. 23:258.

Antolínez-Fernández Á, Esteban-Ramos P, Fernández-Moreno MÁ and Clemente P. 2024. Molecular pathways in mitochondrial disorders due to a defective mitochondrial protein synthesis. Front. Cell Dev. Biol. 12:1410245.

Benson, D. A., M. Cavanaugh, K. Clark, I. Karsch-Mizrachi, D. J. Lipman, J. Ostell, and E. W. Sayers. 2013. GenBank. Nucleic Acids Res. 41:D36–D42.

Bhatti JS, Bhatti GK, Reddy PH. 2017. Mitochondrial dysfunction and oxidative stress in metabolic disorders - A step towards mitochondria based therapeutic strategies. Biochim Biophys Acta Mol Basis Dis. 1863:1066-1077.

Bodenhofer, U., E. Bonatesta, C. Horejš-Kainrath, and S. Hochreiter. 2015. msa: an R package for multiple sequence alignment. Bioinformatics 31:3997–3999.

Bolger AM, Lohse M, Usadel B. 2014.Trimmomatic: a flexible trimmer for Illumina sequence data. Bioinformatics 30: 2114–2120.

Bonferroni, C. E. 1936. Teoria statistica delle classi e calcolo delle probabilità. Pubblicazioni del R Istituto Superiore di Scienze Economiche e Commerciali di Firenze 8:3–62.

Burton, R. S. 2022. The role of mitonuclear incompatibilities in allopatric speciation. Cell. Mol. Life Sci. 79: 103.

Camacho, C., G. Coulouris, V. Avagyan, N. Ma, J. Papadopoulos, K. Bealer, and T. L. Madden. 2009. BLAST+: architecture and applications. BMC Bioinformatics 10:421.

Cao X, Guo L, Zhou C, Huang C, Li G, Zhuang Y, et al. 2023. Effects of N-acetyl-l-cysteine on chronic heat stress-induced oxidative stress and inflammation in the ovaries of growing pullets. Poult. Sci 102, 102274.

Chaudhry A. Mitochondria Analyzer [Software]. 2019. Available from: https://github.com/AhsenChaudhry/Mitochondria-Analyzer

Chen D, McManus CE, Radmanesh B, Matzat LH, Lei EP. 2021. Temporal inhibition of chromatin looping and enhancer accessibility during neuronal remodeling. Nature communications. 12: 6366.

Chen, D., Keremane, S. Wang, S. Lei, E.P. 2025. CTCF regulates global chromatin accessibility and transcription during rod photoreceptor development. PNAS. 122: e2416384122.

Csardi, G., and T. Nepusz. 2006. The igraph software package for complex network research. International Journal Complex Systems. 1695:1–9.

Danecek, P., A. Auton, G. Abecasis, C. A. Albers, E. Banks, M. A. DePristo, R. E. Handsaker, G. Lunter, G. T. Marth, S. T. Sherry, G. McVean, R. Durbin, and 1000 Genomes Project Analysis Group. 2011. The variant call format and VCFtools. Bioinformatics 27:2156–2158.

Danecek, P., J. K. Bonfield, J. Liddle, J. Marshall, V. Ohan, M. O. Pollard, A. Whitwham, T. Keane, S. A. McCarthy, R. M. Davies, and H. Li. 2021. Twelve years of SAMtools and BCFtools. GigaScience 10:giab008.

De Coster, W., S. D'Hert, D. T. Schultz, M. Cruts, and C. Van Broeckhoven. 2018. NanoPack: visualizing and processing long-read sequencing data. Bioinformatics 34:2666–2669.

Edgar, R. C. 2004. MUSCLE: multiple sequence alignment with high accuracy and high throughput. Nucleic Acids Res. 32:1792–1797.

Felsenstein, J. 1981. Skepticism Towards Santa Rosalia, or Why are There so Few Kinds of Animals? Evolution 35:124.

Fick, S. E., and R. J. Hijmans. 2017. WorldClim 2: new 1-km spatial resolution climate surfaces for global land areas. Int. J. Climatol. 37:4302–4315.

Flynn, J. M., R. Hubley, C. Goubert, J. Rosen, A. G. Clark, C. Feschotte, and A. F. Smit. 2020. RepeatModeler2 for automated genomic discovery of transposable element families. Proc. Natl. Acad. Sci. USA 117:9451–9457.

Gabriel, L., T. Brůna, K. J. Hoff, M. Ebel, A. Lomsadze, M. Borodovsky, and M. Stanke. 2024. BRAKER3: fully automated genome annotation using RNA-seq and protein evidence with GeneMark-ETP, AUGUSTUS, and TSEBRA. Genome Res. 34:769–777.

Gerashchenko, M.V. Alexei V. Lobanov, and Vadim N. Gladyshev. 2012. Genome-wide ribosome profiling reveals complex translational regulation in response to oxidative stress. PNAS. 109:17394-17399.

Gompert, Z., and C. A. Buerkle. 2011. Bayesian estimation of genomic clines. Mol. Ecol. 20:2111–2127.

Hansen, M. C., P. V. Potapov, R. Moore, M. Hancher, S. A. Turubanova, A. Tyukavina, D. Thau, S. V. Stehman, S. J. Goetz, T. R. Loveland, et al. 2013. High-resolution global maps of 21st-century forest cover change. Science 342:850–853.

Hill, G. E. 2017. The mitonuclear compatibility species concept. The Auk 134:393–409.

Jeon, S.M., Chandel, N.S., and Hay, N. 2012. AMPK regulates NADPH homeostasis to promote tumour cell survival during energy stress. Nature. 485:661–665.

Keefe, M. S. Levitt, D. E., Vellers, H. L, Benjamin, C. L., Sekiguchi, Y. 2025. Mitochondrial adapations from heat acclimation – A narrative review. J. Therm. Biol. 133:104283.

Khawaja A, Cipullo M, Krüger A et al. 2023. Insights into mitoribosomal biogenesis from recent structural studies.Trends in Biochemical Sciences. 48:629-641

Kim, K.H., Lee, C.B. 2024. Socialized mitochondria: mitonuclear crosstalk in stress. Exp Mol Med. 56:1033–1042.

Kim, D., J. M. Paggi, C. Park, C. Bennett, and S. L. Salzberg. 2019. Graph-based genome alignment and genotyping with HISAT2 and HISAT-genotype. Nat. Biotechnol. 37:907–915.

Kioka H, Kato H, Fujikawa M, Tsukamoto O, Suzuki T, Imamura H, Nakano A, Higo S, Yamazaki S, Matsuzaki T, Takafuji K, Asanuma H, Asakura M, Minamino T, Shintani Y, Yoshida M, Noji H, Kitakaze M,

Kleinberg. J. 1997. Authoritative sources in a hyperlinked environment. *Proc. 9th ACM-SIAM Symposium on Discrete Algorithms*, 1998. Extended version in *Journal of the ACM* 46(1999). Also appears as IBM Research Report RJ 10076.

Komuro I, Asano Y, Takashima S. 2014. Evaluation of intramitochondrial ATP levels identifies G0/G1 switch gene 2 as a positive regulator of oxidative phosphorylation. Proc Natl Acad Sci U S A. 111:273-8.

Kolmogorov, M., J. Yuan, Y. Lin, and P. A. Pevzner. 2019. Assembly of long, error-prone reads using repeat graphs. Nat. Biotechnol. 37:540–546.

Krosby,M., Rohwer,S. 2009. A 2000 km genetic wake yields evidence for northern glacial refugia and hybrid zone movement in a pair of songbirds. Proc. Biol. Sci. 276:615–621.

Larsen S, Nielsen J, Hansen CN, Nielsen LB, Wibrand F, Stride N, et al. 2012. Biomarkers of mitochondrial content in skeletal muscle of healthy young human subjects. J. Physiol 590: 3349–3360.

Lewis CA et al. 2024. Tracing compartmentalized NADPH metabolism in the cytosol and mitochondria of mammalian cells. Mol Cell. 55: 253–263.

Li H, Durbin R. 2009. Fast and accurate short read alignment with Burrows-Wheeler transform. Bioinformatics 25: 1754–1760.

Liu CT, Brooks GA, 2012. Mild heat stress induces mitochondrial biogenesis in C2C12 myotubes. J. Appl. Physiol 112: 354–361.

Love MI, Huber W, Anders S. 2014. Moderated estimation of fold change and dispersion for RNA-seq data with DESeq2. Genome Biol. 15:550.

McShane, E. et al. 2024. A kinetic dichotomy between mitochondrial and nuclear gene expression processes. Demonstrates differences in gene expression kinetics between mitochondria and nucleus, highlighting translation regulation. Mol. Cell. 84: 1541–1555.

Mai, N., Chrzanowska-Lightowlers, Z.M.A. & Lightowlers, R.N. 2017. The process of mammalian mitochondrial protein synthesis. Cell Tissue Res. 367: 5–20.

Makarova K.S., Ponomarev V.A., Koonin E.V. 2001. Two C or not two C: recurrent disruption of Zn-ribbons, gene duplication, lineage-specific gene loss, and horizontal gene transfer in evolution of bacterial ribosomal proteins. Genome Biol. 2: 0033.

Marcos S. Keefea, Danielle E. Levittb, Heather L. Vellersc, Courteney L. Benjamind, Yasuki Sekiguchia,* 2025. Mitochondrial adaptations from heat acclimation – A narrative review. J. Therm. Biol. 133: 104283.

Martin, M. 2011. Cutadapt removes adapter sequences from high-throughput sequencing reads. EMBnet.journal, 17: 10–12.

Moon, S.J., Dong, W., Stephanopoulos, G. N., Sikes, H. D. 2020. Oxidative pentose phosphate pathway and glucose anaplerosis support maintenance of mitochondrial NADPH pool under mitochondrial oxidative stress. Bioengineering & Translational Medicine. 5:e10184.

Muñoz-Garcia, A. Paloma Larraín, Miriam Ben-Hamo, Ariovaldo Cruz-Neto, Joseph B. Williams, Berry Pinshow, Carmi Korine, 2016. Metabolic rate, evaporative water loss and thermoregulatory state in four species of bats in the Negev desert. Comparative Biochemistry and Physiology Part A: Molecular & Integrative Physiology. 191: 156-165.

978 Napolitano, G., Fasciolo, G., & Venditti, P. (2021). Mitochondrial Management of Reactive Oxygen
979 Species. *Antioxidants*, *10*: 1824.

980 Ooms, J. 2014. The jsonlite package: a practical and consistent mapping between JSON data and R
981 objects. arXiv:1403.2805.

982 Oxford Nanopore Technologies. 2018. Medaka: sequence correction provided by ONT Research.
983 Available at https://github.com/nanoporetech/medaka.

984 Patton MG, Gillum TL, Szymanski MC, Gould LM, Lauterbach CJ, Vaughan RA, et al. , 2018. Heat
985 acclimation increases mitochondrial respiration capacity of C2C12 myotubes and protects against LPS-
986 mediated energy deficit. Cell Stress Chaperones. 23, 871–883.

987 Pennycuick, C. J. (1975). Mechanics of flight. In Avian Biology (ed. D. S. Farner), pp.1-75. New York:
988 Academic Press.

989 Pettersen, E. F., T. D. Goddard, C. C. Huang, E. C. Meng, G. S. Couch, T. I. Croll, J. H. Morris, and T. E.
990 Ferrin. 2021. UCSF ChimeraX: structure visualization for researchers, educators, and developers. Protein
991 Sci. 30:70–82.

992 Popov LD, 2020. Mitochondrial biogenesis: an update. J. Cell Mol. Med 24:4892–4899.

993 Quirós, P. M., Mottis, A., & Auwerx, J. 2016. Mitonuclear communication in homeostasis and stress.
994 Nature Reviews Molecular Cell Biology. 17: 213–226.

995 Rahaman, S. et al. 2025. Heat shock induces silent ribosomes and reorganizes mRNA turnover. Cell
996 Reports. 44:116447.

997 Randle, P.J. P. B. Garland, C. N. Hales, & E. A. Newsholme. 1963.The glucose fatty-acid cycle: Its role in
998 insulin sensitivity and the metabolic disturbances of diabetes mellitus. The Lancet. 281: 785–789.

999 Raudvere, U., L. Kolberg, I. Kuzmin, T. Arak, P. Adler, H. Peterson, and J. Vilo. 2019. go:Profiler: a web
1000 server for functional enrichment analysis and conversions of gene lists (2019 update). Nucleic Acids Res.
1001 47:W191–W198.

1002 Raval PK, MacLeod AI, Gould SB .2024. A molecular atlas of plastid and mitochondrial proteins reveals
1003 organellar remodeling during plant evolutionary transitions from algae to angiosperms. PLoS Biol 22:
1004 e3002608.

1005 Rosseel Y. 2012. lavaan: An R package for structural equation modeling. Journal of Statistical Software
1006 48: 1–36.

1007 Salgado RM, Sheard AC, Vaughan RA, Parker DL, Schneider SM, Kenefick RW, et al., 2017.
1008 Mitochondrial efficiency and exercise economy following heat stress: a potential role of uncoupling
1009 protein. Phys. Rep 5: e13054.

1010 Schafer, Z.T., Grassian, A.R., Song, L., Jiang, Z., Gerhart-Hines, Z., Irie, H.Y., Gao, S., Puigserver, P.,
1011 and Brugge, J.S. 2009. Antioxidant and oncogene rescue of metabolic defects caused by loss of matrix
1012 attachment. Nature. 461: 109–113.

1013 Schliep K.P. 2011. phangorn: phylogenetic analysis in R. Bioinformatics, 27: 592-593.

1014 Schliep K.P. 2019. “ape 5.0: an environment for modern phylogenetics and evolutionary analyses in
1015 R.” Bioinformatics. 35: 526-528.

1016 Shen, W., S. Le, Y. Li, and F. Hu. 2016. SeqKit: a cross-platform and ultrafast toolkit for FASTA/Q file
1017 manipulation. PLoS ONE. 11:e0163962.

1018 Sloan, D.B., Havird, J.C. & Sharbrough, J. 2017. The on-again, off-again relationship between
1019 mitochondrial genomes and species boundaries. Molecular Ecology. 26: 2212–2236.

1020 Sokolova, I.M. 2023. Ectotherm mitochondrial economy and responses to global warming. Acta
1021 Physiologica. 237:e13950.

1022 Sonenberg, N., & Hinnebusch, A. G. 2009. Regulation of translation initiation in eukaryotes. Cell, 136:
1023 731–745.

1024 Storz JF. 2016. Hemoglobin-oxygen affinity in high-altitude vertebrates: is there evidence for an adaptive
1025 trend? J Exp Biol. 219:3190-3203.

1026 Swartz, S. Kenneth S. Breuer, David J. Willis. 2008. Aeromechanics in aeroecology: flight biology in the
1027 aerosphere, Integrative and Comparative Biology. 48:85–98.

1028 Swerdlow RH. 2016. Bioenergetics and metabolism: a bench to bedside perspective. J Neurochem.
1029 139:126-135.

1030 Tamura Y, Matsunaga Y, Masuda H, Takahashi Y, Takahashi Y, Terada S, et al. 2014. Postexercise
1031 whole body heat stress additively enhances endurance training-induced mitochondrial adaptations in
1032 mouse skeletal muscle. Am. J. Physiol. Regul. Integr. Comp. Physiol 307: R931–R943.

1033 van den Elzen, Antonia, Helena-Bueno, K., Brown C.R., Chan, L.I., Melnikov, S.V. 2023. Ribosomal
1034 proteins can hold a more accurate record of bacterial thermal adaptation compared to rRNA. Nucleic
1035 Acids Res. 51:8048–8059.

1036 Varadi, M., S. Anyango, M. Deshpande, S. Nair, C. Natassia, G. Yordanova, D. Yuan, O. Stroe, G. Wood,
1037 A. Laydon, et al. 2022. AlphaFold Protein Structure Database: massively expanding the structural
1038 coverage of protein-sequence space with high-accuracy models. Nucleic Acids Res. 50:D439–D444.

1039 Vragović, I., E. Louis, and A. Díaz-Guilera, 2005. Efficiency of informational transfer in regular and
1040 complex networks. Phys. Rev. E 71, 1.

1041 Wakigawa, Taisei et al. 2025. Monitoring the complexity and dynamics of mitochondrial translation .
1042 Molecular Cell. 85: 4279 - 4297.e8.

1043 Wang, S., M. J. Ore, E. K. Mikkelsen, J. Lee-Yaw, D. P. L. Toews, S. Rohwer, and D. Irwin. 2021.
1044 Signatures of mitonuclear coevolution in a warbler species complex. Nat. Commun. 12:4279.

1045 Wang, S., Mank, J.E., Ortiz-Barrientos, D. & Rieseberg, L.H. 2025. Genome architecture and speciation
1046 in plants and animals. Molecular Ecology. 34: e70004.

1047 Wasserman, S., and Faust, K. 1994. Social Network Analysis: Methods and Applications. Cambridge:
1048 Cambridge University Press.

1049 Wickham, H. 2023. httr: tools for working with URLs and HTTP. R package version 1.4.7. https://CRAN.R-
1050 project.org/package=httr.

Wiens, J. J., & Graham, C. H. 2005. Niche conservatism: Integrating evolution, ecology, and conservation biology. Annual Review of Ecology, Evolution, and Systematics. 36: 519–539.

Yang Liao, Gordon K. Smyth, Wei Shi. 2014. featureCounts: an efficient general purpose program for assigning sequence reads to genomic features, *Bioinformatics*. 30:923–930.

Youngflesh, C., Saracco, J.F., Siegel, R.B. et al. 2022. Abiotic conditions shape spatial and temporal morphological variation in North American birds. Nat Ecol Evol 6:1860–1870.